An Electrometer Design and Characterization for a CubeSat Neutral Pressure Instrument

Todd Rohrer

Thesis submitted to the Faculty of the
Virginia Polytechnic Institute and State University
in partial fulfillment of the requirements for the degree of

Master of Science
in
Electrical Engineering

Gregory D. Earle, Chair
Daniel M. Sable
Anbo Wang

November 29, 2016
Blacksburg, Virginia

Keywords: Space, Spacecraft, CubeSat, Instrumentation, Analog Circuit Design

An Electrometer Design and Characterization for a CubeSat Neutral Pressure Instrument

Todd Rohrer

ABSTRACT

Neutral gas pressure measurements in low Earth orbit (LEO) can facilitate the monitoring of atmospheric gravity waves, which can trigger instabilities that severely disrupt radio frequency communication signals. The Space Neutral Pressure Instrument (SNeuPI) is a low-power instrument that determines neutral gas pressure by detecting neutral gas density. SNeuPI utilizes an ionization chamber, an ion detector, and a logarithmic electrometer. The Rev. 1 SNeuPI electrometer prototype does not function as designed. A Rev. 2 electrometer circuit must be designed and its performance characterized across specified operating temperature and input current ranges.

This document presents a design topology for the Rev. 2 electrometer and a derivation of its theoretical transfer function. Component selection and layout are discussed. A range of predicted operating input currents is calculated using modeled neutral density data for a range of local times, altitudes, and latitudes corresponding to the conditions expected for the Lower Atmosphere/Ionosphere Coupling Experiment (LAICE) CubeSat mission. Laboratory test setups for measurements performed both under vacuum and at atmospheric pressure are documented in detail. Test procedures are presented to characterize the performance of the Rev. 2 electrometer at a range of controlled operating temperatures. The results of these tests are then extrapolated in order to predict the operation of the circuit at specified temperatures outside of the range controllable under laboratory test conditions. The logarithmic conformance, accuracy, sensitivity, power consumption, and deviations from expected response of the circuit are characterized. The results validate the electrometer for use under its expected flight conditions.

An Electrometer Design and Characterization for a CubeSat Neutral Pressure Instrument

Todd Rohrer

GENERAL AUDIENCE ABSTRACT

Neutral gas pressure measurements in low Earth orbit (LEO) can facilitate the monitoring of atmospheric gravity waves, oscillations that transfer energy from weather events or other disturbances through the atmosphere and can severely disrupt radio frequency communication signals. The Space Neutral Pressure Instrument (SNeuPI) is a low-power instrument detecting neutral gas density in order to determine neutral gas pressure. SNeuPI is part of the instrument payload for the Lower Atmosphere/Ionosphere Coupling Experiment (LAICE). LAICE is a CubeSat–a small satellite format utilizing commercial off-the-shelf (COTS) parts to minimize development cycle time and cost–developed with the goal of observing atmospheric gravity waves. SNeuPI utilizes an ionization chamber, which ionizes neutral gas molecules, an ion detector that ouputs an electron current proportional to ion density, and an electrometer circuit, which outputs a voltage logarithmically related to the magnitude of the detector electron current. The Rev. 1 SNeuPI electrometer prototype does not function as designed. A Rev. 2 electrometer circuit must be designed and its performance characterized across specified operating temperature and input current ranges.

This document presents a circuit design for the Rev. 2 electrometer and a mathematical derivation of the relationship between its input current and output voltage. Component selection and layout are discussed. A range of predicted operating input currents is calculated using modeled neutral density data for a range of local times, altitudes, and latitudes corresponding to the conditions expected for the LAICE mission. Laboratory test setups for measurements performed both under vacuum and at atmospheric pressure are documented in detail. Test procedures are presented to characterize the performance of the Rev. 2 electrometer at a range of controlled operating temperatures. The results of these tests are then extrapolated in order to predict the operation of the circuit at specified temperatures outside of the range controllable under laboratory test conditions. The logarithmic conformance, accuracy, sensitivity, power consumption, and deviations from expected response of the circuit are characterized. The results validate the electrometer for use under its expected flight conditions.

Dedication

To my daughter, Fiona Bloomquist Rohrer, my wife, Abbie Bloomquist Rohrer, and my parents, Dennis and Wendy Rohrer.

Acknowledgments

I would like to give special thanks to Dr. Gregory Earle and Stephen Noel for their encouragement, guidance, and constructive criticism. I would like to thank Vidur Garg, whose work designing the SNeuPI instrument has formed the foundation for this research, and Ellen Robertson, whose diligent assistance and keen insight have been invaluable throughout the process of building, testing, and troubleshooting the SNeuPI circuitry. I would also like to thank Lee Kordella for his generosity in sharing his impressive knowledge and laboratory testing skills. Lastly, I would like to express my sincere thanks and appreciation to my wife, Abbie Bloomquist Rohrer, whose unwavering support has made this endeavor possible.

This research has been carried out in support of NASA grant NNM16AA11A and NSF grant AGS-1242898.

Unless otherwise noted, all photos by author, 2016.

Contents

List of Figures

List of Tables

List of Acronyms

ADC analog to digital converter

APD Advanced Performance Detector

COTS commercial off-the-shelf

DMM digital multimeter

EMI electromagnetic interference

DE-2 Dynamics Explorer-2

GPIB IEEE-488 General Purpose Interface Bus

GUI graphical user interface

IC integrated circuit

IGS Ionization Gauge Sensor

LAICE Lower Atmosphere/Ionosphere Coupling Experiment

LIIB LAICE Instrument Interface Board

LINAS LAICE Ionization Gauge Neutral Atmosphere Sensor

LEO low Earth orbit

MCP microchannel plate

PCB printed circuit board

PCS Keithley model 6220 precision current source

SNeuPI Space Neutral Pressure Instrument

SRI Stanford Research Institute

TCR temperature coefficient of resistance

VI virtual instrument

Chapter 1

Introduction

In situ measurement of neutral gas density and pressure in low Earth orbit (LEO) requires instrumentation with a high degree of accuracy and sensitivity over a wide range of operating conditions. Ambient neutral density and temperature may vary significantly over the course of a single satellite orbit. In order to collect and meaningfully interpret data from this dynamic environment, engineers and scientists must understand and characterize the impact of changing physical factors on the performance of sensors and electronics.

Gravity waves, oscillations that transfer energy from weather events or other disturbances through the atmosphere and ionosphere, can trigger instabilities that severely disrupt radio frequency communication signals. Measurements of neutral and plasma density can enable observation of gravity wave propagation. The data measured by the Dynamics Explorer-2 (DE-2) satellite, launched in 1981, illustrate this potential. Figure 1.1 shows ion and neutral density data from orbit 8250 of DE-2. Note that the ion and neutral density fluctuations are anticorrelated, which is consistent with the fact that these measurements were made below the F-peak, where the neutral density gradient is negative with increasing altitude and the ion density gradient is positive with increasing altitude (Earle et al., 2008).

Such density measurements, in combination with mesospheric airglow sensor data, have the potential to facilitate the correlation of ionospheric gravity waves with tropospheric weather systems. The Lower Atmosphere/Ionosphere Coupling Experiment (LAICE) is a CubeSat–a small satellite format utilizing commercial off-the-shelf (COTS) parts to minimize development cycle time and cost. The LAICE mission, a cooperative effort of Virginia Tech and the University of Illinois, will be the first satellite with a mid-inclination orbit to combine these measurements in a focused study of gravity wave propagation in the mesosphere, thermosphere, and ionosphere (Westerhoff et al., 2015).

The LAICE satellite payload includes two neutral pressure instruments: the Space Neutral Pressure Instrument (SNeuPI) and the LAICE Ionization Gauge Neutral Atmosphere Sensor (LINAS). LINAS, a Bayard-Alpert type hot-filament ionization gauge, exceeds the power

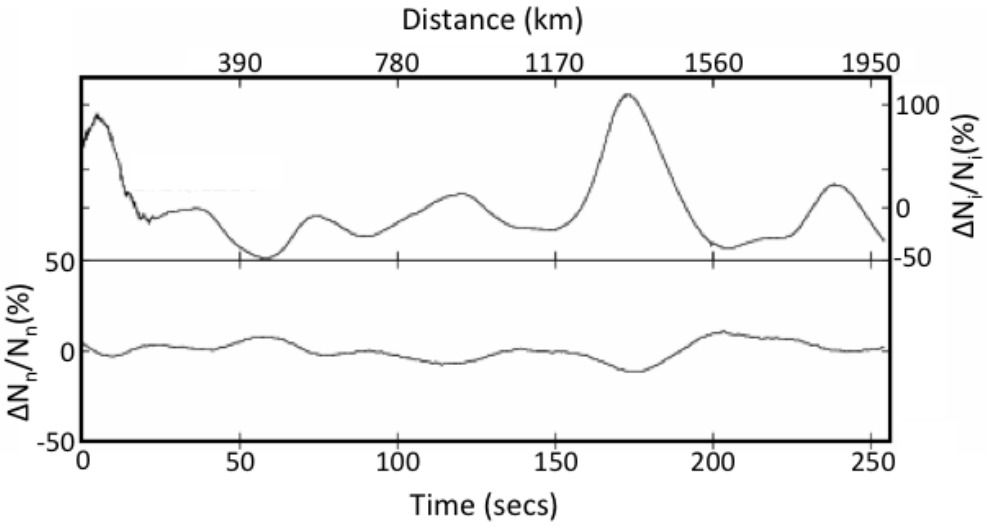

Figure 1.1: Data from orbit 8250 of the DE-2 satellite. Anticorrelated ion and neutral density wave structures are shown in top and bottom panels, respectively. Image courtesy of Gregory Earle.

budget of the CubeSat format in continuous operation, but can be operated in a pulsed mode in order to validate the functionality of SNeuPI. SNeuPI is an experimental low-power design prototype that does not use thermionic filaments as its ionization source. The LAICE mission will therefore also serve as a technology demonstration for the SNeuPI design.

The SNeuPI instrument design utilizes a novel combination of a Spindt microtip emitter device (Spindt et al., 2001) and a microchannel plate (MCP) device to ionize neutral gases and generate an electron current output linearly related to the environmental neutral gas density. This electron current is then measured by an electrometer circuit, which outputs an analog voltage proportional to the logarithm of the current. This signal is further conditioned and input into an analog to digital converter (ADC) in order to be downlinked and processed with the rest of the LAICE data (Garg, 2015). Figure 1.2 shows a simulation of particle trajectories in the SNeuPI accommodation chamber generated using the SIMION software tool. Figure 1.3 depicts a high-level functional block diagram of the SNeuPI instrument.

One challenge to both the effective design of the SNeuPI instrument and the accurate analysis of its measured data is the wide range of temperatures over which the instrument must operate. The satellite will spend half of every 90-minute orbit in darkness, and the angle of incident light will vary throughout the illuminated half of each orbit depending on time, solar zenith angle, season, and which segments of the satellite are exposed to the sun. The target operational temperature range of the SNeuPI instrument is $-20\,^{\circ}\mathrm{C}$ to $75\,^{\circ}\mathrm{C}$. While LAICE will have an on-board heating device that will be deployed in the event of extreme low temperatures, the complexity and power requirements of implementing fine temperature control are prohibitive for the CubeSat format.

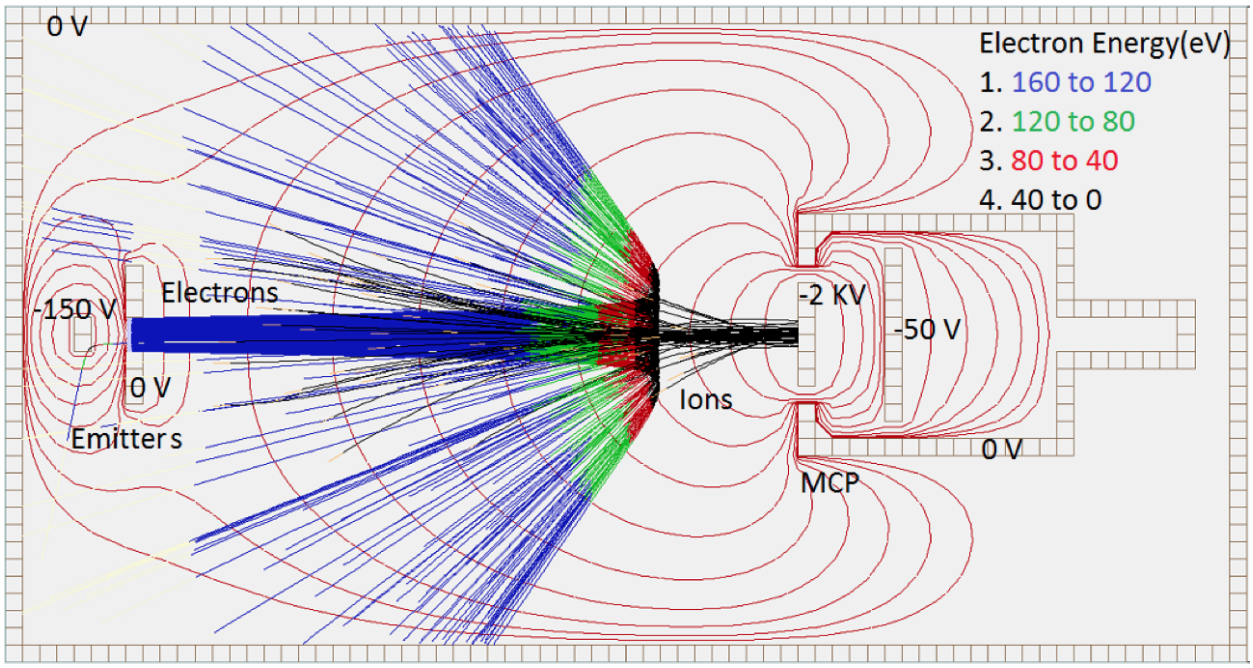

Figure 1.2: A drawing showing simulated particle trajectories in the SNeuPI accommodation chamber. Vidur Garg. *Swept Neutral Pressure Instrument (SNeuPI): investigating gravity waves in the ionosphere.* 2015. Master's thesis, Virginia Polytechnic Institute and State University. Used by permission.

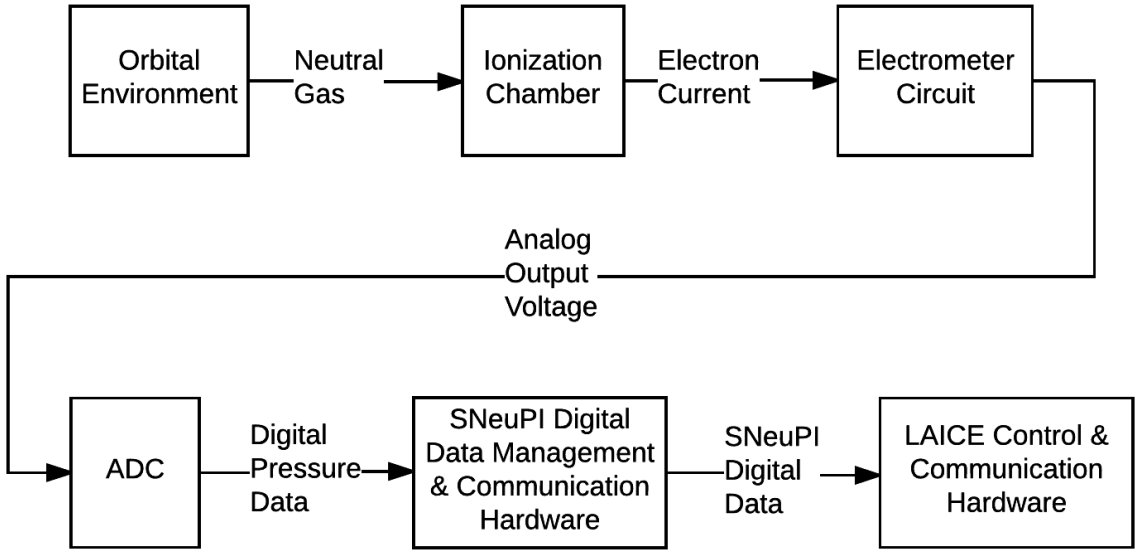

Figure 1.3: A high-level block diagram of the SNeuPI instrument showing data flow from neutral gas density to instrument digital output.

This work is concerned primarily with documenting the design, testing, and performance of the SNeuPI electrometer circuit, with a particular focus on characterizing uncertainty due to temperature and other factors. Because the sensistivity, accuracy, and uncertainty of each of the SNeuPI instrument's functional blocks will directly impact the certainty of any conclusions made on the basis of its measurements, it is desirable to characterize these qualities wherever possible. These results will, in turn, be examined in order to characterize the error in pressure measurements due to any deviations in electrometer circuit performance. The key objectives for this work are outlined below.

Objectives:

1. Design and build a transimpedance logarithmic amplifier to measure MCP electron current over a range corresponding to the expected in situ neutral pressure over the duration of the LAICE mission.

2. Measure the accuracy and sensitivity of the electrometer circuit at sampled temperatures over its specified operating range.

3. Develop an algorithm for predicting circuit performance as a continuous function of temperature.

4. Characterize deviations from expected circuit response and quantify the resulting measurement error.

5. Determine and document best practices for designing, building, and testing noise- and leakage current-sensitive circuits for the benefit of future researchers.

Chapter 2

Literature Review

2.1 The Bayard-Alpert Ionization Gauge

The Bayard-Alpert ionization gauge was conceived by Robert Bayard and Daniel Alpert in 1950, and has seen common use in laboratory vacuum test environments since. This type of gauge directly measures neutral gas flux, which is proportional to pressure for a given gas species at a known temperature. The gauge utilizes a hot filament to generate an electron current, which flows to a grid anode biased to a higher potential. A number of these electrons proportional to the neutral gas density inside the gauge collide with neutral molecules, producing positively-charged ions. These ions are then drawn to a negatively-biased (with respect to the filament) collector electrode, which outputs a current proportional to neutral pressure (Bayard and Alpert, 1950). Figure 2.1 depicts a Bayard-Alpert type ionization gauge used in the Space@VT vacuum lab.

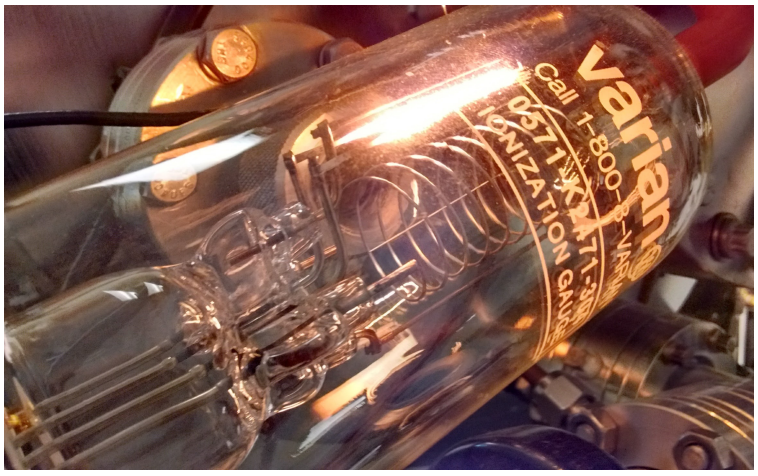

Figure 2.1: Close-up of a Bayard-Alpert type ionization gauge tube connected to the Space@VT vacuum chamber. Note the glowing hot filament electron source.

The LINAS gauge to be flown on the LAICE satellite utilizes an ionization gauge of the Bayard-Alpert type. The specific sensor used in the LINAS design is based upon the Ionization Gauge Sensor (IGS), developed by The Aerospace Corporation and used previously on the STREAK satellite mission (Westerhoff et al., 2015; Clemmons et al., 2009).

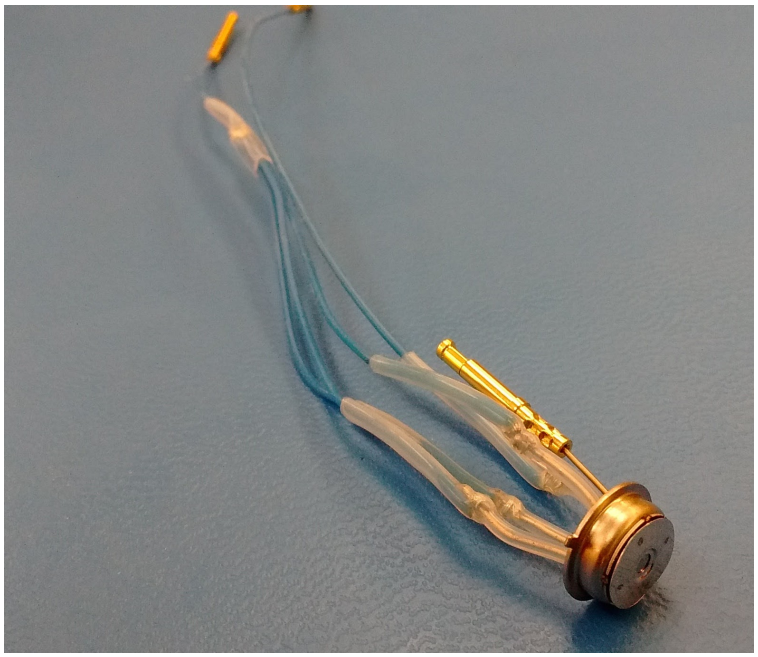

Figure 2.2: A Spindt microtip cathode device with SNeuPI wiring harness.

2.2 The Spindt Microtip Emitter

The Spindt microtip emitter is a cold-cathode electron emission device originally developed by the Stanford Research Institute (SRI) in the late 1960s (Spindt, 1968). The device utilizes an array of conductive metal conical tips connected to a base electrode at evenly spaced intervals on the order of micrometers. A second electrode, known as a "gate," is positioned over the tip array such that each tip is aligned with an aperture in the gate. This assembly is mounted in a TO-5 package; Figure 2.2 shows a Spindt cathode device connected to the SNeuPI wiring harness. When a sufficiently large negative potential (with respect to the gate) is applied to the tip electrode, field electron emission occurs (Spindt et al., 2001). Fowler and Nordheim (1928) describe the phenomenon of cold-cathode field emission in thorough detail.

2.3 Microchannel Plate Current Amplifier

Chevron-oriented MCP devices have been employed since the early 1970s in various instrumentation applications, often as photomultipliers (Catchpole and Johnson, 1970; Colson et al., 1970). Such a device consists of two thin biased plates, each containing an array of

micrometer-scale tubelike channels. The channels within each plate are oriented parallel to each other and at an angle to the plane of the plate surface such that when the two plates are stacked together at 180 degrees rotation, the channels form a chevron pattern as viewed from a cross-sectional side view (see Figure 2.3). Each channel functions as an electron multiplier tube, such that a current of particles or photons impinging upon the outer surface of the first plate is amplified by the cascading effect of electrons flowing through the chevron-oriented channels. The device outputs the amplified electron current from an electrode connected to the outer surface of the second plate. The amplification factor of the device is dependent upon the differential bias voltage between the two plates. The MCP device employed in the SNeuPI instrument design, shown in Figure 2.4, is part of the Advanced Performance Detector (APD) line of products from Photonis (Garg, 2015; Photonis USA, Inc., nd).

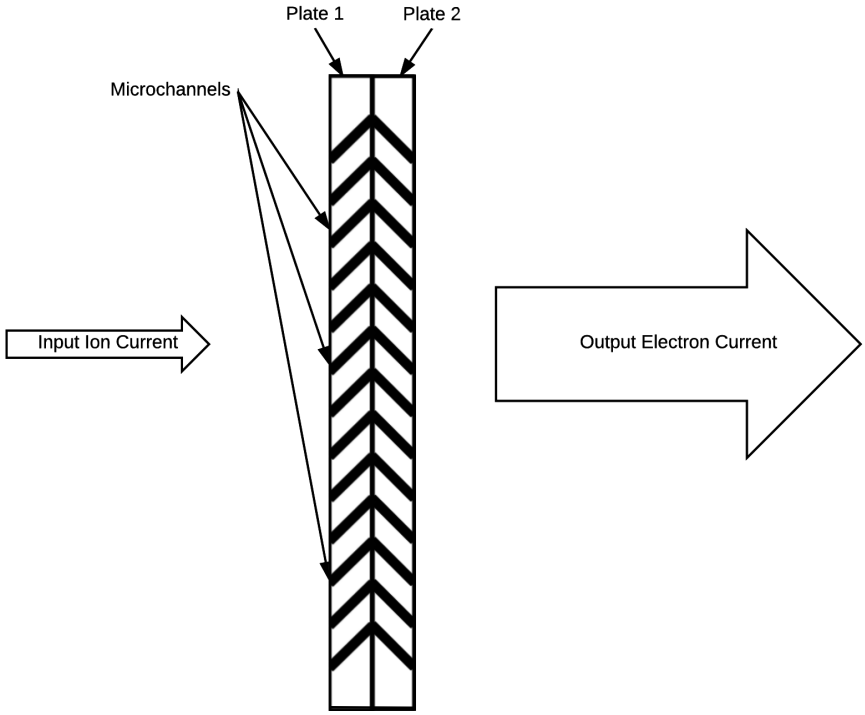

Figure 2.3: A simplified cross-sectional diagram of an MCP device as used in the SNeuPI ionization chamber. A current of positively charged ions strikes the surface of Plate 1 and is amplified into a much larger electron current by the electron multiplication effect of the microchannels. Diagram is not to scale.

2.4 The SNeuPI Instrument

Like the Bayard-Alpert ionization gauge, SNeuPI measures neutral pressure by ionizing neutral gas molecules at a rate proportional to neutral density and measuring the resultant ion current. SNeuPI, however, accomplishes this task with lower power consumption due to its utilzation of a cold-cathode Spindt emitter device, as described in Section 2.2. Neutral gas

Figure 2.4: A Photonis APD microchannel plate device as used in the SNeuPI ionization chamber.

molecules enter the accommodation chamber housing the SNeuPI and LINAS instruments, shown in Figures 2.5 and 2.6, through a small ram-facing aperture. A baffle attached to the underside of the accommodation chamber lid divides the chamber between the SNeuPI and LINAS gauges, as shown in Figure 2.7. The neutral gas inside the chamber reaches equlibrium at a pressure related to environmental neutral gas pressure according to the ram effect (Garg, 2015). Hanson et al. (1992) describes the process of calculating equilibrium pressure for a chamber with a ram-facing aperture; Section 5.2 of this document presents such calculations for the SNeuPI instrument in detail.

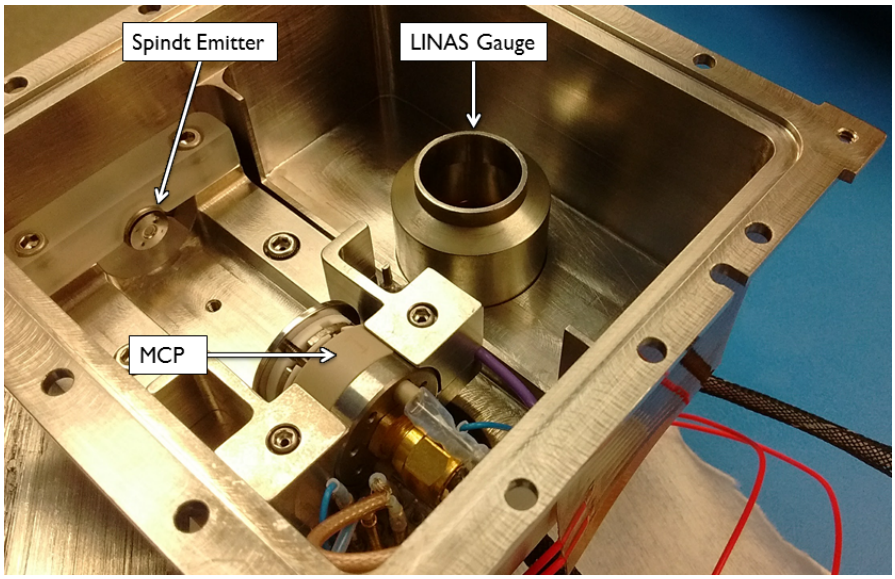

Figure 2.5: The SNeuPI/LINAS accomodation chamber. The SNeuPI ionization chamber is in the foreground; the LINAS gauge is visible in the background.

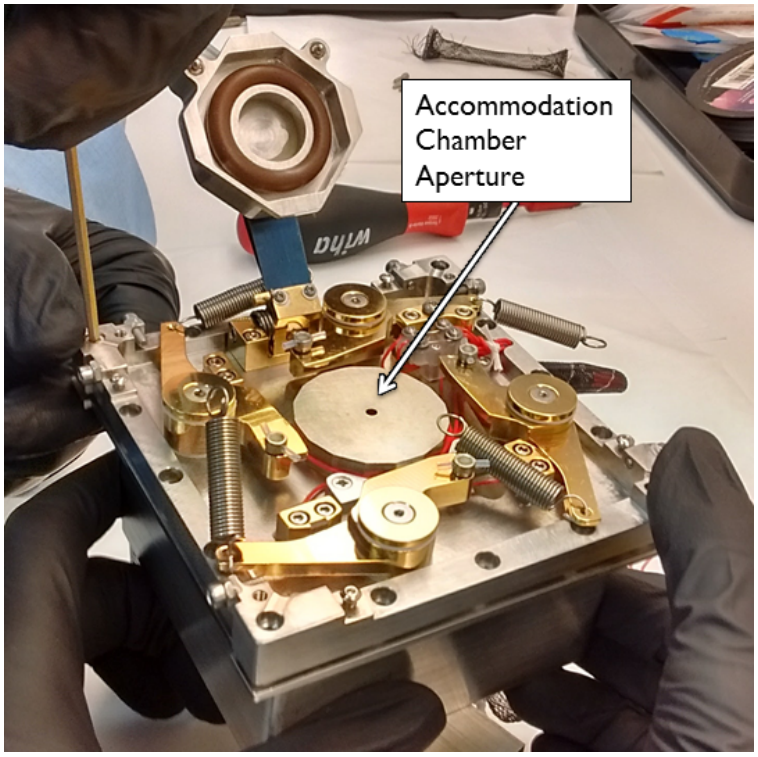

Figure 2.6: The SNeuPI/LINAS accomodation chamber with the lid installed.

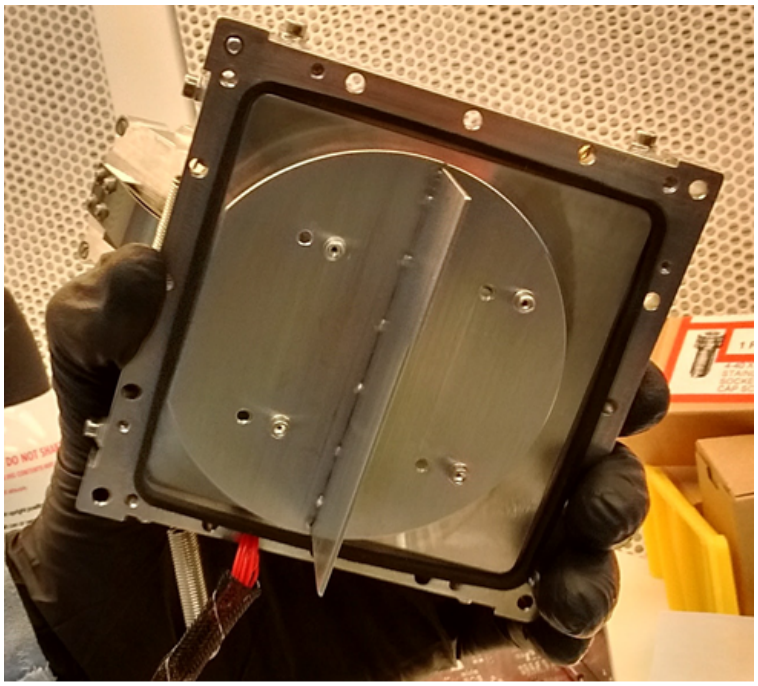

Figure 2.7: The underside of the accommodation chamber lid with the dividing baffle in place.

The electron stream from the microtip emitter collides with neutral gas molecules inside the ionization chamber, creating positively-charged ions. The rate of ionization within the chamber is related to neutral gas density, electron emission current, and the ionization efficiency of the emitted electrons (Garg, 2015). Ions generated by this process are attracted to the front plate of the MCP, which is biased at $-1.5\,\mathrm{kV}$. The second plate is biased at $-40\,\mathrm{V}$. The amplified electron current is output via an SMA connector integrated into the MCP device housing (Garg, 2015). Figure 2.8 illustrates the ionization process.

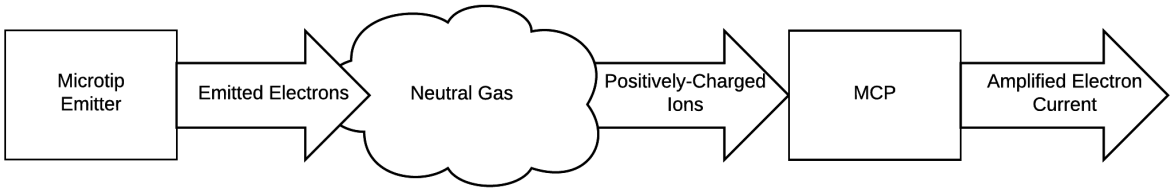

Figure 2.8: A high-level functional diagram of the SNeuPI ionization chamber.

The SNeuPI electronics are implemented on three printed circuit boards (PCBs): an FPGA control and communication board, shown in Figure 2.9, an emitter current control board, shown in Figure 2.10, and the electrometer board, shown in Figure 2.11 (Garg, 2015). The FPGA and emitter control boards are mounted in Lok-Tainer$^{\mathrm{TM}}$ retaining slots attached to the LAICE chassis, as shown in Figure 2.12. The electrometer board is mounted on standoffs to the LAICE Instrument Interface Board (LIIB), which interfaces control, power management, and data link functions between the Space@VT payload and the LAICE satellite flight computer.

Rev. 1 of the SNeuPI electrometer circuit, as designed by Garg (2015), utilizes a Texas Instruments/Burr-Brown LOG114 monolithic logarithmic amplifier. This chip meets all of the requirements specified for the SNeuPI logarithmic amplifier, but is designed to accept positive-polarity input currents. In order to adapt the LOG114 for use in the electrometer circuit, Garg employs a basic current inverter circuit in series with the amplifier input, as suggested by the LOG114 datasheet for negative-polarity current measurement applications. However, the Rev. 1 prototype does not function properly over the four lowest-valued decades of specified input currents, as shown in Figure 2.13. After a considerable amount of time was spent in attempting to troubleshoot this circuit, the decision was made to design a negative-input logarithmic amplifier from the ground up. The need to design, validate, and characterize the Rev. 2 electrometer motivates the remainder of this work.

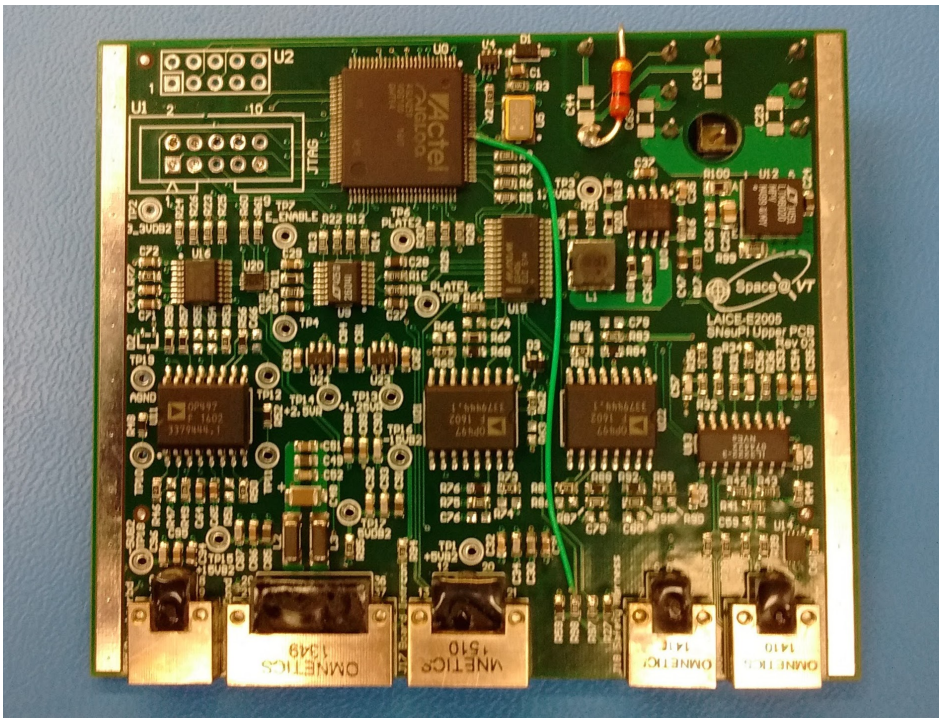

Figure 2.9: The SNeuPI FPGA PCB.

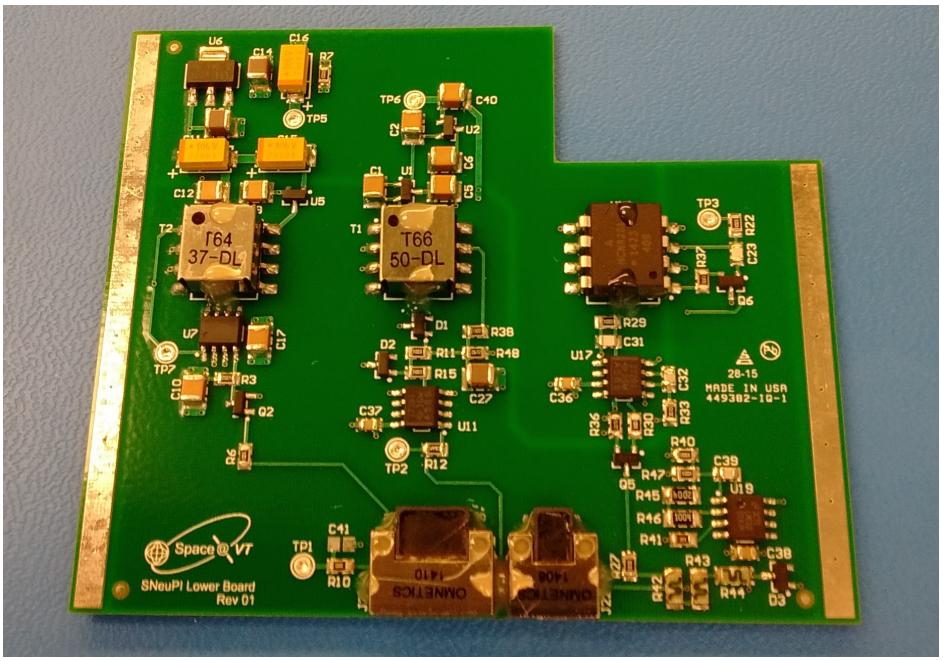

Figure 2.10: The SNeuPI emitter control PCB.

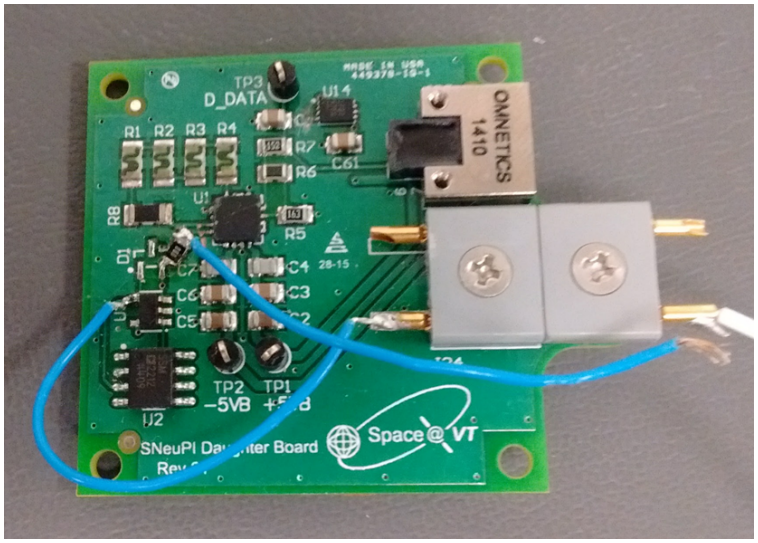

Figure 2.11: The SNeuPI electrometer Rev. 1 prototype.

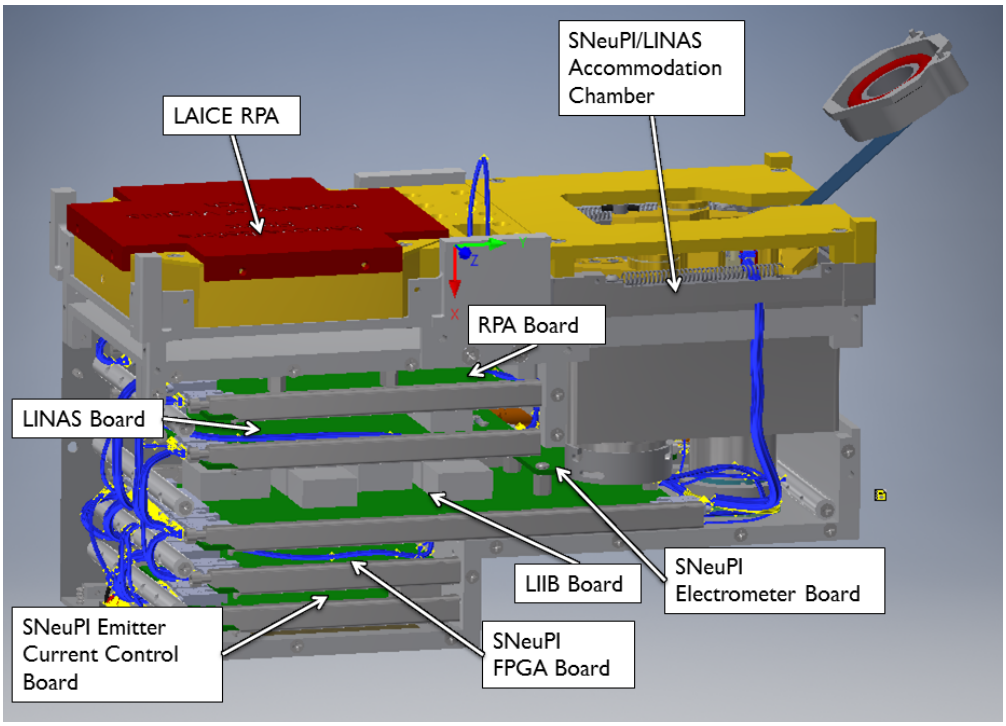

Figure 2.12: CAD model image of the LAICE chassis showing the SNeuPI PCBs and accommodation chamber. The LAICE RPA, which will measure ion density and temperature, is also pictured.

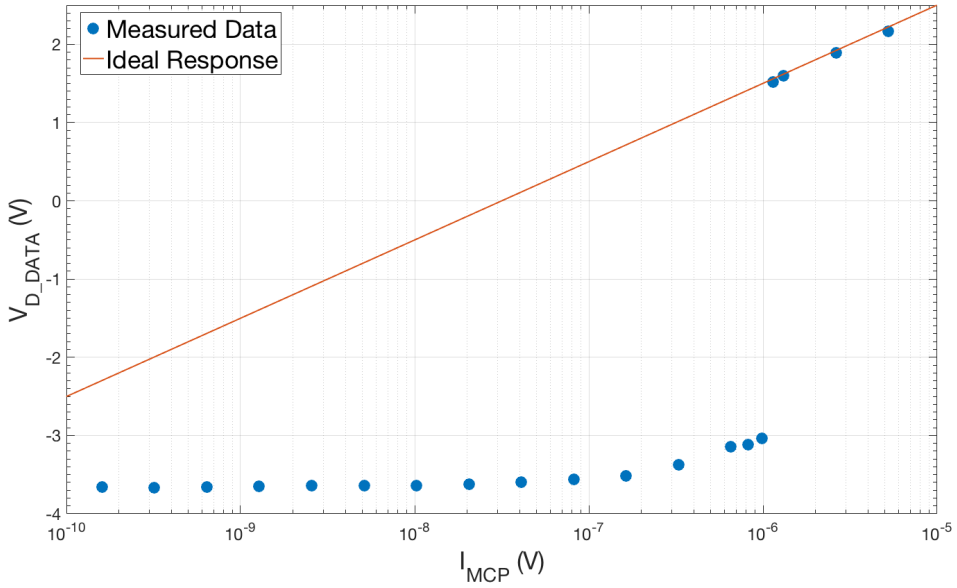

Figure 2.13: Data from the Rev. 1 electrometer circuit. Note the deviation from expected behavior over the bottom four decades of input current.

Chapter 3

Electrometer Design

3.1 Rev. 2 Electrometer Circuit Topology

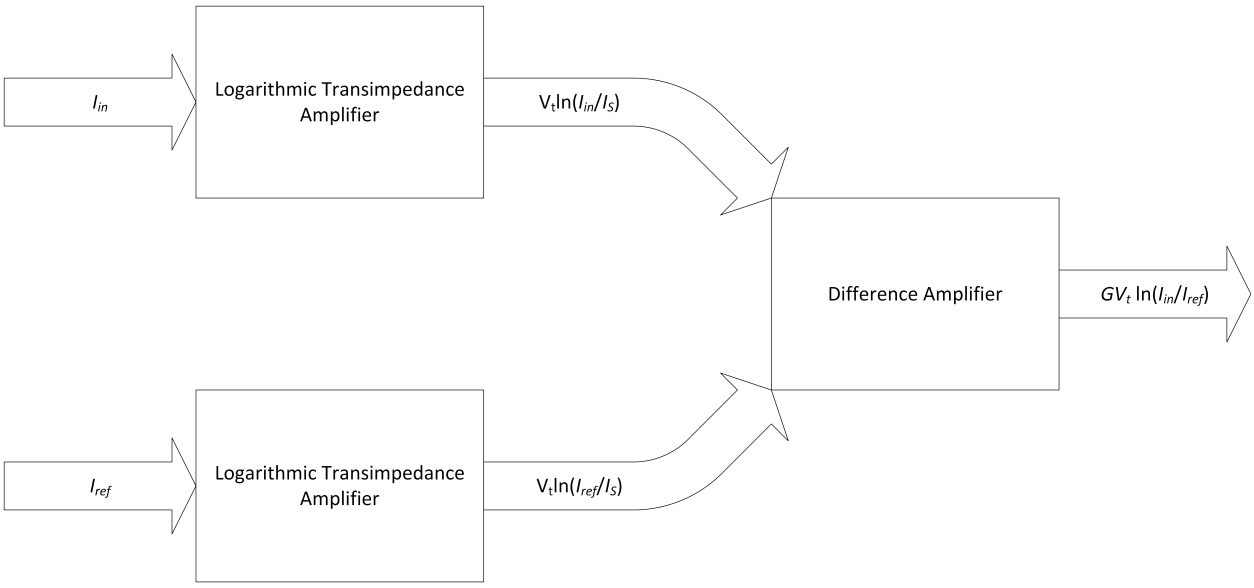

Figure 3.1: A simplified LOG114 block diagram (Texas Instruments Incorporated, 2007).

In considering different logarithmic amplifier topologies, several key factors were considered, including input current range, circuit bandwidth over the input current range, temperature compensation, and parts availability. Circuits requiring stability compensation capacitors at the input stage were rejected due to poor circuit bandwidth at low input currents. Temperature compensation schemes utilizing positive temperature coefficient of resistance (TCR) resistors were investigated but abandoned due to the lack of availability of such devices in the values needed. A topology was selected that provides a limited degree of temperature

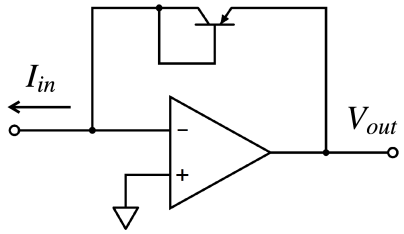

Figure 3.2: A simple op amp logarithmic transimpedance amplifier stage. The diode-connected transistor is PNP type in order to measure negative input currents, and I_{in} is represented as a positive current flowing out of the input terminal.

compensation, with the expectation that additional processing of measurement data would be necessary to fully compensate for temperature dependencies.

The topology of the Rev. 2 logarithmic amplifier is based on an internal circuit diagram for the LOG114 as depicted in the datasheet for that device (Texas Instruments Incorporated, 2007). Figure 3.1 depicts a simplified block diagram of this circuit. The input stage consists of two transimpedance logarithmic amplifier subcircuits, each essentially a simple transimpedance amplifier with a diode-connected transistor replacing its feedback resistor, as shown in Figure 3.2. The polarity of this transistor depends on the polarity of the input currents to be measured. The LOG114 uses NPN transistors in its logarithmic amplifier stage in order to measure positive input currents, while the Rev. 2 electrometer circuit uses PNP transistors in order to measure negative input currents.

As Figure 3.1 shows, the input of one of the two logarithmic amplifier stages is connected to a known reference current, determined by the value of an external resistor between an on-chip 2.5 V reference and the inverting input of the operational amplifier (op amp), which is held at ground under normal operating conditions. The input of the other logarithmic amplifier stage is connected to the current being measured. The outputs of these two input amplifier stages are connected to the inputs of a differential amplifier stage, the output of which the user may optionally connect to an additional noninverting amplifier stage (not shown) integrated into the LOG114 chip. Due to the quotient property of logarithms, shown in Equation 3.1, the output of the differential amplifier stage is equal to the scaled logarithm of the ratio of the input current to the reference current.

$$\ln(A) - \ln(B) = \ln\left(\frac{A}{B}\right) \tag{3.1}$$

3.2 Transfer Function Derivations

Figures 3.3 and 3.4 respectively depict simplified schematics of the Rev. 2 electrometer circuit and the FPGA board analog circuitry considered in the following DC transfer func-

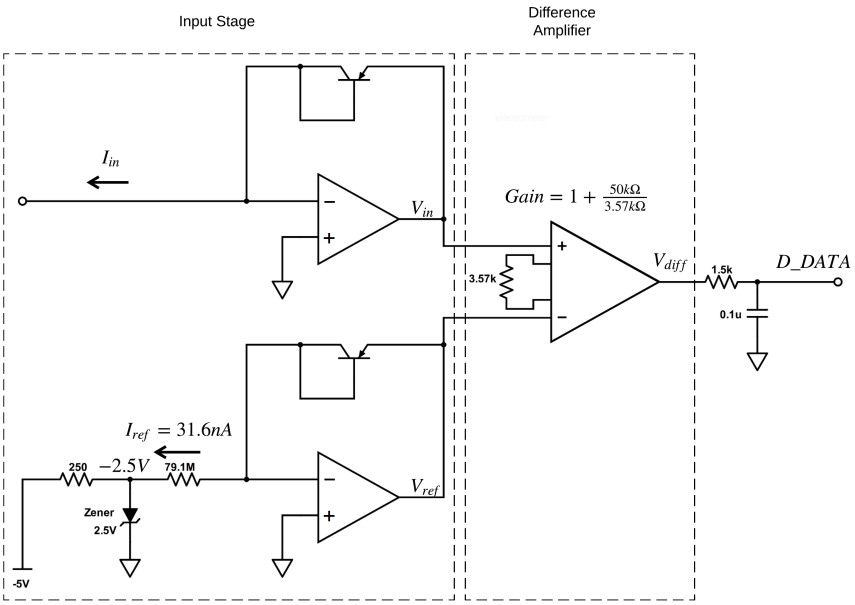

Figure 3.3: A simplified Rev. 2 electrometer circuit schematic.

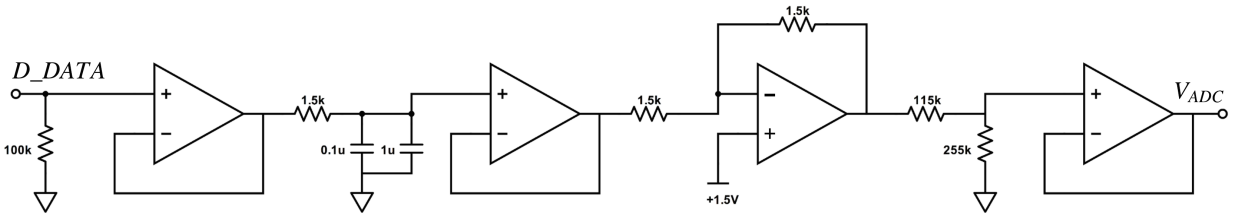

Figure 3.4: FPGA board analog circuitry, as considered in the transfer function derivation.

tion derivation. Complete schematics for the electrometer and FPGA board circuitry are shown in Appendix C, Figures C.1 and C.2, respectively. The electrometer input (I_{in}) and reference (I_{ref}) currents will be treated as positive currents flowing out of the circuit's input terminals (rather than negative currents flowing into the input terminals) in accordance with standard electrical engineering practice. This convention will be maintained for purposes of data analysis throughout the remainder of this document. In the following derivation, V_{in} represents the output voltage of the input logarithmic amplifier stage, V_{ref} represents the output voltage of the reference logarithmic amplifier stage, V_{diff} represents the differential amplifier output voltage, and V_{ADC} represents the input voltage to the FPGA board ADC (the signal designated as D_DATA_ADC in the full FPGA board schematic). This derivation will ignore frequency response characteristics of the circuit. This is justified because both

lowpass filter cutoff frequencies are above the signal bandwidth of interest for this design (0.5 Hz due to the ADC sample averaging period of 1 s). All op amp input impedances are assumed to be infinite, and all op amp output impedances are assumed to be zero.

The diode-connected PNP transistors will be treated as simple diodes. The relationship between forward-biased voltage and current can then be closely approximated using the Schockley ideal diode equation:

$$I_D = I_S \left(e^{V_D / V_T} - 1 \right), \tag{3.2}$$

where I_D is the forward current of the diode, I_S is the reverse saturation current of the diode, V_D is the forward-biased voltage of the diode, and V_T is thermal voltage.

Rearranging Equation 3.2:

$$V_D = V_T \ln \left(\frac{I_D}{I_S} + 1 \right). \tag{3.3}$$

This derivation assumes that I_D is much larger than I_S. This assumption may not always be valid in real-world design scenarios, and its validity in the present application is not certain. An I_S specification is not readily available for the MAT03 dual transistor selected for the input stage, and the integrated reverse-bias protection diodes of the device preclude direct measurement of the parameter (Analog Devices, Inc., 2002). Any deviations in the final design test data from the expected response may warrant further consideration of the validity of this assumption.

Then

$$\frac{I_D}{I_S} + 1 \approx \frac{I_D}{I_S}. \tag{3.4}$$

Thus,

$$V_D \approx V_T \ln \left(\frac{I_D}{I_S} \right). \tag{3.5}$$

Assuming that the op amp outputs are not saturating, the inverting inputs can each be assumed to be at ground potential due to the noninverting inputs being tied to ground. The output voltage of each op amp is therefore equal to the forward-biased voltage drop of the transistor diode in its negative feedback loop. Because a single package containing two closely-matched transistors is used to implement the feedback diodes in both input stage amplifiers, the reverse saturation currents of the two devices can be assumed to be equal.

The significance of this equivalence will soon become apparent. The output voltages of the two input stage amplifiers are

$$V_{in} = V_T \ln\left(\frac{I_{in}}{I_S}\right) \tag{3.6}$$

and

$$V_{ref} = V_T \ln\left(\frac{I_{ref}}{I_S}\right). \tag{3.7}$$

The difference amplifier stage is implemented using a Texas Instruments INA121 instrumentation amplifier. According to the device datasheet (Burr-Brown, 1998) the gain of this amplifier is set by the value of an external gain-setting resistor (R_G). The gain equation is

$$Gain_{diff} = 1 + \frac{50\,\mathrm{k\Omega}}{R_G}. \tag{3.8}$$

In the SNeuPI electrometer circuit, R_G is set to 3.57 kΩ. Thus,

$$Gain_{diff} = 1 + \frac{50\,\mathrm{k\Omega}}{3.57\,\mathrm{k\Omega}}. \tag{3.9}$$

The transfer function of the differential amplifier stage is therefore

$$V_{diff} = \left(1 + \frac{50\,\mathrm{k\Omega}}{3.57\,\mathrm{k\Omega}}\right)(V_{in} - V_{ref}). \tag{3.10}$$

Substituting Equations 3.6 and 3.7 into Equation 3.10 and rearranging yields

$$V_{diff} = V_T \left(1 + \frac{50\,\mathrm{k\Omega}}{3.57\,\mathrm{k\Omega}}\right)\left[\ln\left(\frac{I_{in}}{I_S}\right) - \ln\left(\frac{I_{ref}}{I_S}\right)\right]. \tag{3.11}$$

Applying logarithmic properties and simplifying yields

$$V_{diff} = V_T \left(1 + \frac{50\,\mathrm{k\Omega}}{3.57\,\mathrm{k\Omega}}\right) \ln\left(\frac{\frac{I_{in}}{I_S}}{\frac{I_{ref}}{I_S}}\right) \tag{3.12}$$

$$= V_T \left(1 + \frac{50\,\mathrm{k\Omega}}{3.57\,\mathrm{k\Omega}}\right) \ln\left(\frac{I_{in}}{I_{ref}}\right). \tag{3.13}$$

This result illustrates one of the primary advantages of this circuit topology: the use of a matched transistor pair to implement the input stage feedback diodes enables the elimation of the I_S term from the transfer function. Because diode reverse saturation current is heavily temperature-dependent, this strategy provides a degree of temperature compensation to the circuit's performance. The thermal voltage dependency, however, remains; its effects are compensated for using the data-processing algorithm detailed in Section 5.5.

The loading due to the 100 kΩ resistor to ground at the D_DATA node of the FPGA circuit creates a voltage divider at DC with the 1.5 kΩ resistor from the preceding lowpass filter:

$$V_{D\_DATA} = \left(\frac{100\,\mathrm{k\Omega}}{100\,\mathrm{k\Omega} + 1.5\,\mathrm{k\Omega}}\right) V_{diff} \tag{3.14}$$

$$= V_T \left(\frac{100\,\mathrm{k\Omega}}{100\,\mathrm{k\Omega} + 1.5\,\mathrm{k\Omega}}\right) \left(1 + \frac{50\,\mathrm{k\Omega}}{3.57\,\mathrm{k\Omega}}\right) \ln\left(\frac{I_{in}}{I_{ref}}\right). \tag{3.15}$$

In order to compare this theoretical transfer function with laboratory test results using curve-fitting tools in MATLAB (see Chapter 5), it is desirable to convert the transfer function to the following standard form:

$$V_{ADC} = a \ln\left(I_{in}\right) + b. \tag{3.16}$$

Then

$$V_{D\_DATA} = A\left[\ln\left(I_{in}\right) + \ln\left(\frac{1}{I_{ref}}\right)\right] \tag{3.17}$$

$$= A\ln\left(I_{in}\right) + A\ln\left(\frac{1}{I_{ref}}\right), \tag{3.18}$$

where

$$A = V_T \left(\frac{100\,\mathrm{k\Omega}}{100\,\mathrm{k\Omega} + 1.5\,\mathrm{k\Omega}}\right) \left(1 + \frac{50\,\mathrm{k\Omega}}{3.57\,\mathrm{k\Omega}}\right). \tag{3.19}$$

At 300 K (approximately room temperature),

$$V_T \approx 25.85\,\mathrm{mV}. \tag{3.20}$$

Substituting this value into Equation 3.19 yields

$$A \approx 0.3822. \tag{3.21}$$

Substituting this value and the designed I_{ref} value of 31.6 nA into 3.18 yields

$$V_{D\_DATA}|_{temp=300\,\mathrm{K}} = 0.3822 \ln(I_{in}) + 6.600. \tag{3.22}$$

D_DATA is followed by two unity-gain buffers, and the third gain stage on the FPGA board inverts the signal and uses a 1.5 V reference to generate a 2.5 V offset. A voltage divider before the final ADC driver gain stage attenuates the signal in order to protect the ADC input from over- or under-voltage conditions. This voltage divider was added in the third revision of the circuit after the clamping diode-based protection scheme of the previous revisions proved insufficient to protect the ADC from certain fault conditions. The final transfer function is thus determined as follows:

$$\begin{aligned} V_{ADC} &= (-V_{D\_DATA} + 2.5\,\mathrm{V}) \left(\frac{255\,\mathrm{k\Omega}}{255\,\mathrm{k\Omega} + 115\,\mathrm{k\Omega}} \right) && (3.23) \\ &= B \left[-A \ln \left(\frac{I_{in}}{I_{ref}} \right) + 2.5\,\mathrm{V} \right] && (3.24) \\ &= B \left\{ -A \left[\ln(I_{in}) - \ln(I_{ref}) \right] + 2.5\,\mathrm{V} \right\} && (3.25) \\ &= -AB \ln(I_{in}) + B \left[A \ln(I_{ref}) + 2.5\,\mathrm{V} \right], && (3.26) \end{aligned}$$

where

$$B = \frac{255\,\mathrm{k\Omega}}{255\,\mathrm{k\Omega} + 115\,\mathrm{k\Omega}} \approx 0.6892. \tag{3.27}$$

Then

$$V_{ADC}|_{temp=300\,\mathrm{K}} \approx -0.2634 \ln(I_{in}) - 2.826, \tag{3.28}$$

again using the designed I_{ref} value of 31.6 nA.

The temperature compensation algorithm detailed in Section 5.5 will make extensive use of calibration curve best-fit equations of the form

$$I_{in} = c(T)\, e^{d(T) V_{ADC}}, \tag{3.29}$$

with the goal of determining the temperature dependencies $c(T)$ and $d(T)$. It is therefore worthwhile to rearrange the theoretical transfer function to fit this form. Letting

$$K = \frac{A}{V_T} = \left(\frac{100\,\mathrm{k\Omega}}{100\,\mathrm{k\Omega} + 1.5\,\mathrm{k\Omega}} \right) \left(1 + \frac{50\,\mathrm{k\Omega}}{3.57\,\mathrm{k\Omega}} \right) \approx 14.78 \tag{3.30}$$

yields

$$V_{ADC} = -BKV_T \ln\left(I_{in}\right) + B\left[KV_T \ln\left(I_{ref}\right) + 2.5\,\mathrm{V}\right] \tag{3.31}$$

and

$$\frac{V_{ADC} - B\left[KV_T \ln\left(I_{ref}\right) + 2.5\,\mathrm{V}\right]}{-BKV_T} = \ln\left(I_{in}\right). \tag{3.32}$$

Therefore,

$$I_{in} = exp\left(\frac{V_{ADC} - B\left[KV_T \ln\left(I_{ref}\right) + 2.5\,\mathrm{V}\right]}{-BKV_T}\right) \tag{3.33}$$

$$= exp\left(\frac{-B\left[KV_T \ln\left(I_{ref}\right) + 2.5\,\mathrm{V}\right]}{-BKV_T}\right) exp\left(\frac{V_{ADC}}{-BKV_T}\right), \tag{3.34}$$

$$c\left(T\right) = exp\left(\frac{-B\left[KV_T \ln\left(I_{ref}\right) + 2.5\,\mathrm{V}\right]}{-BKV_T}\right) \tag{3.35}$$

$$= exp\left(\ln\left(I_{ref}\right) + \frac{2.5\,\mathrm{V}}{KV_T}\right) \tag{3.36}$$

$$= I_{ref} exp\left(\frac{2.5\,\mathrm{V}}{KV_T}\right) \tag{3.37}$$

and

$$d\left(T\right) = \frac{-1}{BKV_T}. \tag{3.38}$$

In the equations above,

$$V_T = kT, \tag{3.39}$$

where

$$k \approx 8.617 \times 10^{-5}\,\frac{\mathrm{eV}}{\mathrm{K}} \tag{3.40}$$

is Boltzmann's constant.

Substituting the values from Equations 3.27, 3.30, 3.39, and 3.40 into Equation 3.37 and simplifying yields

$$c\left(T\right) = \left(31.6 \times 10^{-9}\right) exp\left(\frac{1.962 \times 10^{3}}{T}\right). \tag{3.41}$$

Substituting the values from Equations 3.27, 3.30, 3.39, and 3.40 into Equation 3.38 and simplifying yields

$$d\left(T\right) = \frac{-1.139 \times 10^{3}}{T}. \tag{3.42}$$

SNeuPI temperature data will be measured and processed in units of degrees Celsius, so Equations 3.41 and 3.42 can be written as

$$c\left(T_C\right) = \left(31.6 \times 10^{-9}\right) exp\left(\frac{1.962 \times 10^{3}}{T_C + 273.15}\right). \tag{3.43}$$

$$d\left(T_C\right) = \frac{-1.139 \times 10^{3}}{T_C + 273.15}. \tag{3.44}$$

3.3 Component Selection

The need to measure currents on the order of 100 pA necessitates careful selection of the components used in implementing this design. Most significantly, the input stage op amps need to have extremely small input bias currents. The Texas Instruments LMC6482 is specified to have a typical input bias current of 20 fA at 25 °C, and a maximum input bias current of 4 pA at the extremes of its −40 °C–85 °C operating junction temperature range (Texas Instruments Incorporated, 2015).

Another factor crucial to the proper function of this circuit is the matching of the input stage transistor pair. As described in Section 3.2, the reverse saturation current term I_S only cancels out of the transfer function if the parameters of the two transistors are very closely matched. The Analog Devices MAT03 device is a dual PNP transistor pair implemented on a single chip to achieve close matching. The bulk resistance of the device is typically about 0.3 Ω, enabling excellent logarithmic conformance (Analog Devices, Inc., 2002).

In selecting components, an effort was made to locate components with lead-plated leads. Lead-free components have been known to grow single-crystal conductuve structures called tin whiskers (Sampson, 1998). Tin whiskers sometimes form between component terminals and other conductive surfaces in a circuit, and may lead to component or system failure. Most modern components are only available in COTS form in lead-free packaging, so there were very few leaded component options for the electrometer circuit. The MAT03 transistor,

however, is still available from certain vendors with lead-plated leads. This factor motivated the selection of the obsolete MAT03 over its lead-free-only successor, the Analog Devices SSM2220.

3.4 Electrometer PCB Layout

The SNeuPI electrometer circuit is laid out using a four-layer PCB. Most of the circuit components and signal traces are located on the top of the board. The entire second layer acts as a ground plane, and the third layer is split between the 5 V and −5 V supply rails. A small number of components and signal traces are located on the bottom of the PCB. Due to the low bandwidth requirement of the elctrometer circuit, no special attention was paid to capacitance between traces, although groups of parallel traces in close proximity were avoided. Considering the magnitudes of current flowing in the circuit, the use of a ground plane, a split power plane, and wide power supply traces in the top signal layer should be sufficient to prevent any problems related to fluctuations in power and ground potential due to unwanted impedances. There may, however, be cause for concern about the possibility of measurement errors for input currents near the low end of the specified electrometer range. The magnitude of leakage currents on the surface of the PCB between circuit nodes could likely become significant compared to input currents in this range.

In order to address this possible vulnerability, the input current from the MCP is connected to the electrometer circuit using a Winchester connector, which keeps the input signal isolated from the PCB surface (see Figure 3.5). The circuit node connecting the Winchester connector to the input transistor and op amp input terminals is also insulated from the PCB surface. The solder joint at this node is connected to the top of a Teflon-insulated post epoxied to the PCB, with the op amp input terminal pin bent up to make the connection off-board. The TO-78 package housing the input stage transistor pair is mounted upside-down in order to place its input leads close to this connection point.

A Linear Technology LTC2997 temperature sensor integrated circuit (IC) is included on the SNeuPI electrometer board. This chip was utilized in the initial design for both the electrometer and FPGA boards to collect temperature data for the circuits (Garg, 2015). These data will prove essential in accurately analyzing electrometer measurement data collected in flight, as described in Section 5.5.

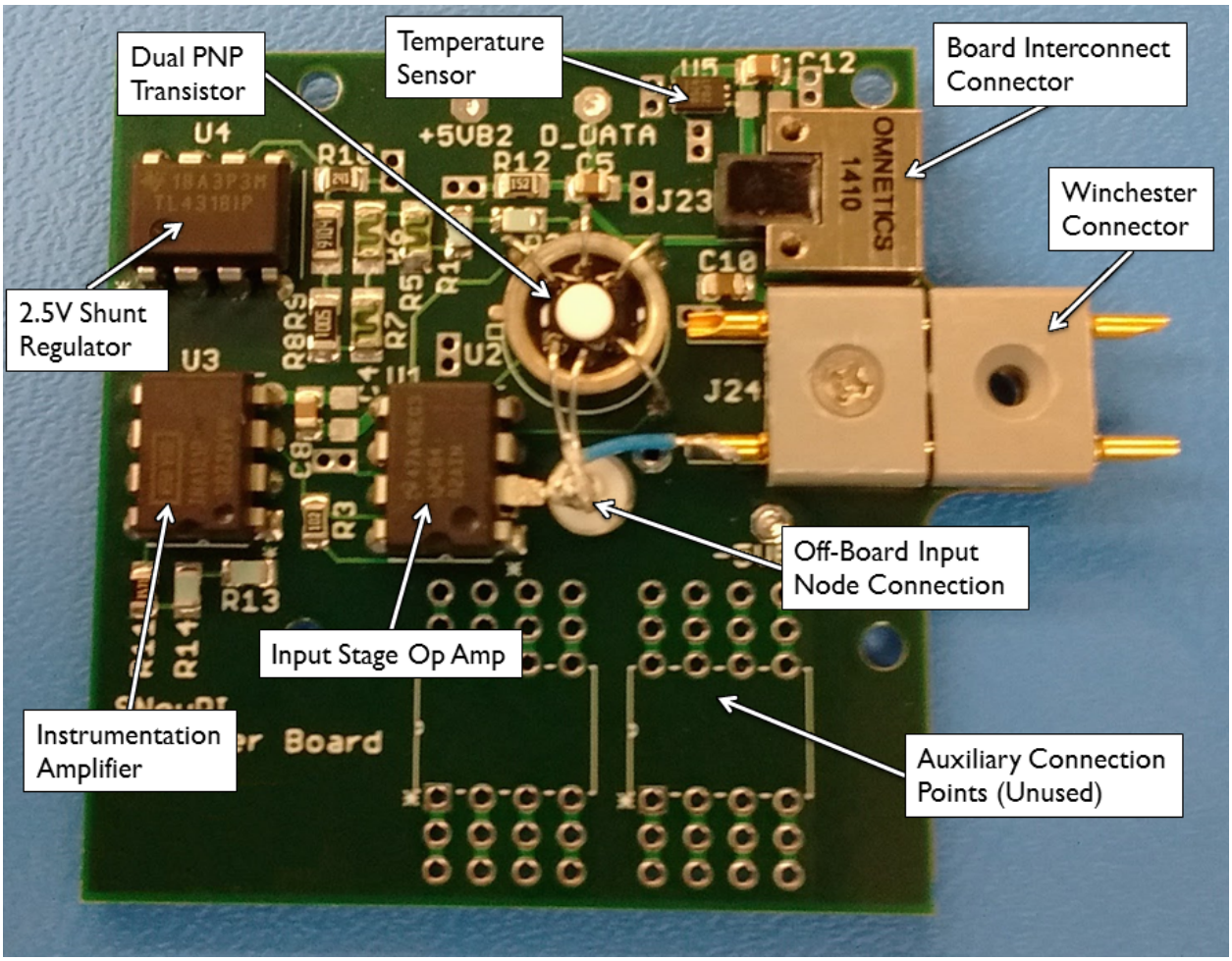

Figure 3.5: The SNeuPI electrometer Rev. 2 PCB.

Chapter 4

Test Setup and Methods

4.1 Testing Goals and Motivation

4.1.1 Pressure Calibration

In order to extract meaningful information from flight data, it is desirable to characterize the relationship between I_{MCP} and accommodation chamber pressure. In order for I_{MCP} data measured by the electrometer in flight to be translated into neutral gas pressure measurements, the relationship between neutral pressure and I_{MCP} must be empirically determined using an experimental setup approximating the flight environment as closely as possible.

4.1.2 Logarithmic Conformance

An important metric for evaluating the success of the SNeuPI electrometer design will be the logarithmic conformance of the implemented circuit, determined by the relationship between measured V_{D_DATA} output voltage (defined in Chapter 3) and test input current magnitude. The performance of the electrometer in this regard will directly impact the SNeuPI instrument accuracy over the full range of specified input currents. Any deviation in the circuit response from logarithmic conformance will be characterized as a percent error relative to the ideal predicted behavior. This test will be performed at room temperature using a Keithley model 6220 precision current source (PCS) to generate test currents.

4.1.3 Temperature Calibration

Temperature-dependent effects, such as the thermal voltage dependency of the electrometer transfer function and the potentially unpredictable behavior of circuit components, can reasonably be expected to significantly impact the output of the circuit over the wide specified operating temperature range of the SNeuPI instrument. In order to accurately analyze flight data, the electrometer circuit response must be determined as a function of temperature. The goal of the temperature calibration test is to observe the performance of the electrometer

circuit at controlled operating temperatures ranging from room temperature to the top end of the specified temperature range.

4.1.4 Power Consumption

Another important metric of the success of the electrometer design is the power consumption of the circuit. Due to the equipment limitations of the Space@VT laboratory, the simplest way to determine whether the SNeuPI instrument operates within its power budget as previously designed is to compare the power consumption of the Rev. 2 electrometer with that of the Rev. 1 circuit. This can be accomplished by comparing the current output from the $\pm 5\,\mathrm{V}$ power supplies for the duration of a sweep of sampled points over the specified input current range for both circuits.

4.2 Laboratory Equipment Setup

4.2.1 Vacuum Chamber Test Setup and Control

The pressure calibration test must obviously be performed under vacuum, while the electrometer circuit tests may be performed at atmospheric pressure. However, due to the extremely small input currents at the low end of the specified electrometer range, measurement inaccuracies caused by electromagnetic interference (EMI) noise can be significant. In order to mitigate this problem, the logarithmic conformance and temperature calibration tests will also be conducted with the electrometer circuit inside the Space@VT vacuum chamber, shown in Figure 4.1. For these tests, the chamber will simply function as a Faraday cage.

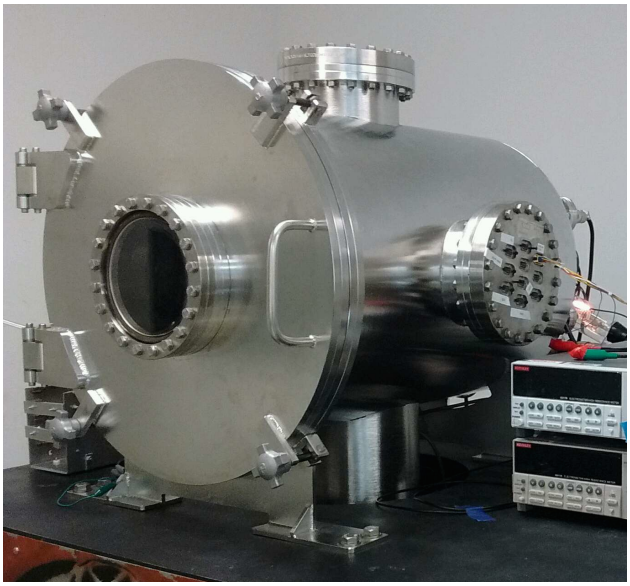

Figure 4.1: An external view of the Space@VT vacuum chamber. Note D-subminiature feedthroughs on the side of the chamber.

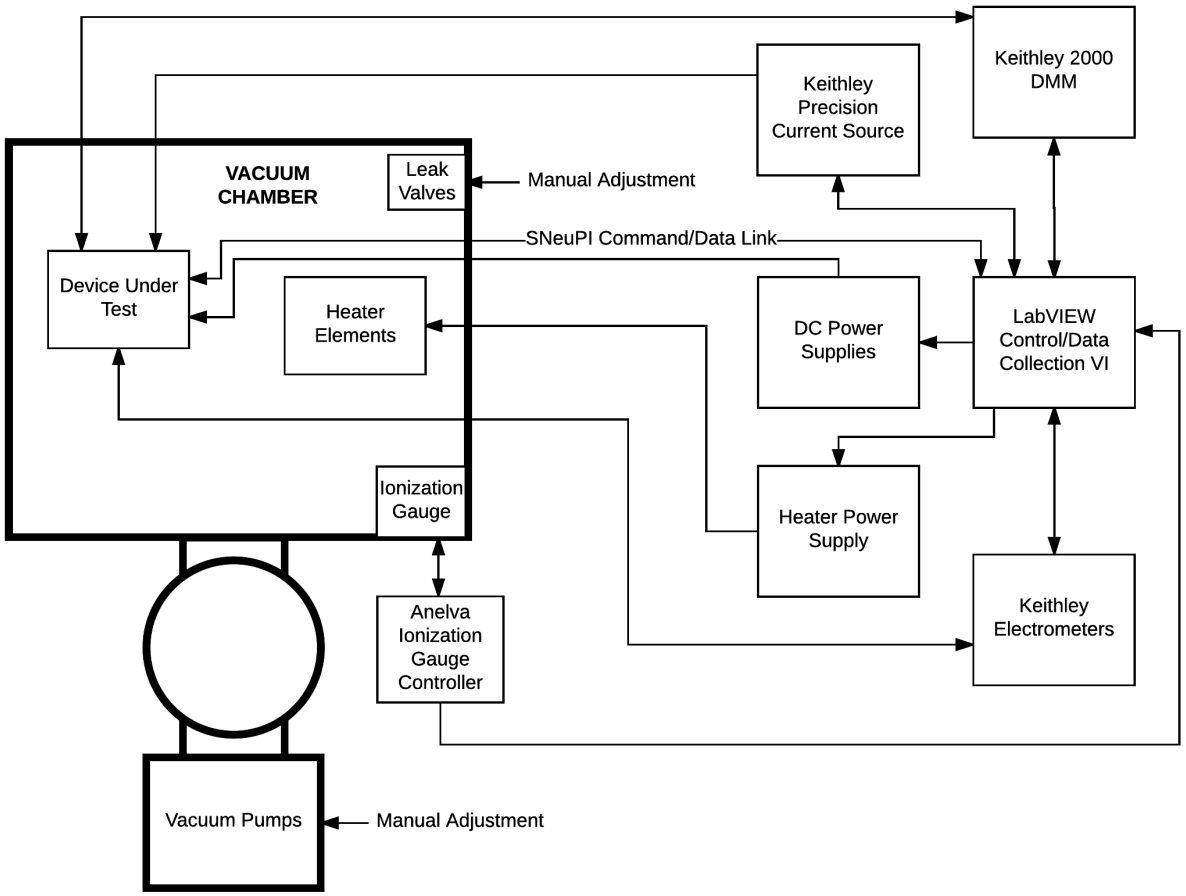

Figure 4.2: Block diagram of the vacuum chamber test setup.

Figure 4.2 shows a block diagram of the vacuum chamber test equipment setup. The FPGA and emitter control PCBs are mounted on Lok-Tainer^{TM} board retaining brackets attached to a test chassis, which is placed on the platform inside the vacuum chamber. The electrometer PCB sits on standoffs on a nickel plate placed on the vacuum chamber platform. All laboratory instruments are located outside the vacuum chamber, and all instrument leads are connected to the devices under test via the D-subminiature feedthroughs on the side of the vacuum chamber. Figure 4.3 shows an interior view of the vacuum chamber setup for the electrometer board tests.

Various manually-adjusted DC power supplies are used according to the voltage and current requirements of the different tests. Additional benchtop instruments include Keithley model 6517A and 6517B precision electrometers, a Keithley PCS, a Keithley model 2000 digital multimeter (DMM), and an Agilent 6035A high voltage DC power supply, all connected to the laboratory computer via IEEE-488 General Purpose Interface Bus (GPIB).

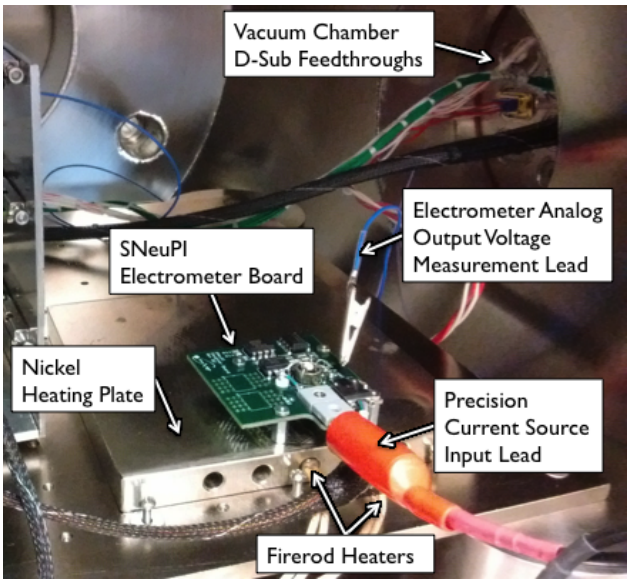

Figure 4.3: Vacuum chamber interior test setup.

Digital control and data collection functions are performed by a LabVIEW virtual instrument (VI) running on the laboratory computer. All laboratory instruments measuring test data or requiring real-time control interface with this VI. The VI also communicates with the SNeuPI FPGA, and its front panel graphical user interface (GUI) accepts user input and displays measurement data and instrument status to the user in real time. Figure 4.4 shows a screenshot of the front panel.

The vacuum chamber pumps are operated manually by the system user. A Bayard-Alpert type ionization gauge connected to the vacuum chamber measures ambient vacuum chamber pressure; pressure measurements are digitized by an Anelva M-833HG ionization gauge controller and communicated via RS-232 serial bus to the control VI. The vacuum chamber leak valve, which is connected to a pressurized dry nitrogen tank, can be adjusted manually by the system user to vary the pressure in the chamber.

4.2.2 Temperature Control

The Agilent 6035A power supply is connected to two Watlow FIREROD^{TM} resistive heaters (see Figure 4.5), which are placed into cylindrical channels drilled into the nickel plate upon which the electrometer PCB sits. The plate serves as a heat sink for the FIRERODs, such that heat radiated to the underside of the PCB and conducted through the standoffs is distributed as evenly as possible. Figure 4.6 shows a closeup view of the nickel plate with FIREROD^{TM} inserted. f

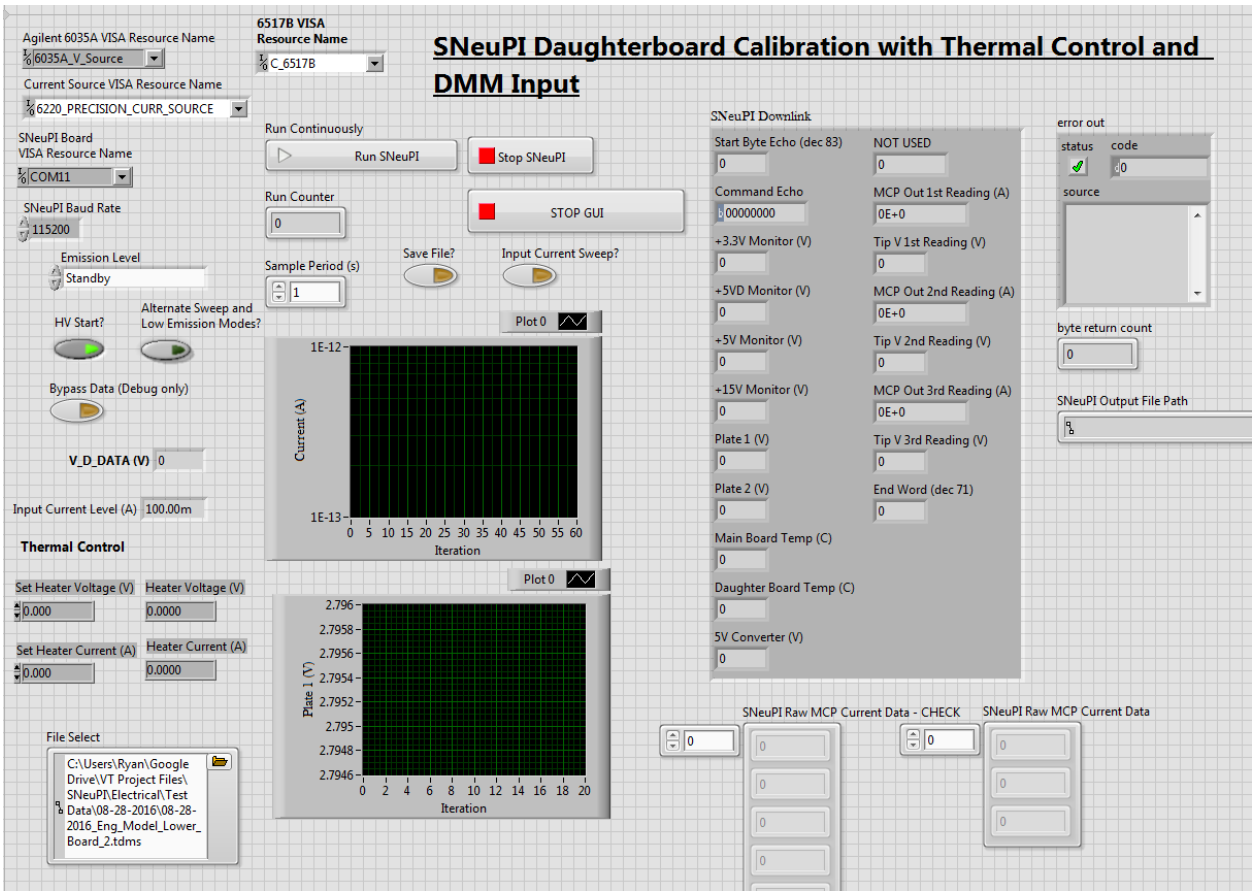

Figure 4.4: Screenshot of electrometer test LabVIEW front panel GUI.

Figure 4.5: FIREROD^{TM} resistive heaters.

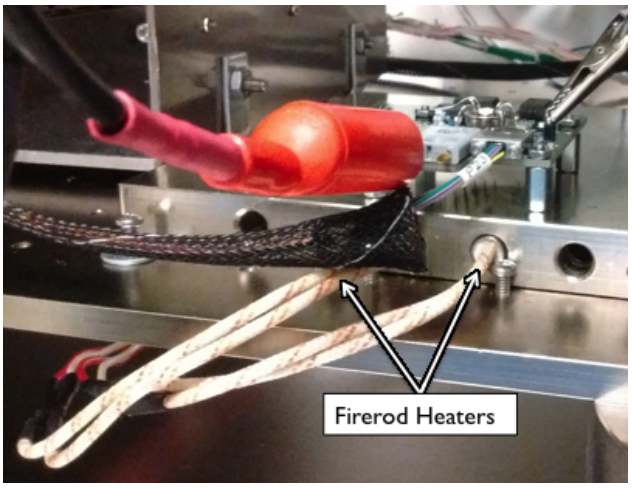

Figure 4.6: Vacuum chamber electrometer test setup showing a clearer view of FIREROD^{TM} heaters in position.

4.3 Testing Procedure

4.3.1 Pressure Calibration Procedure

Figure 4.7 shows a functional block diagram indicating the flow of data and control for the pressure calibration test. The microtip emitter and MCP are placed in a test proxy box approximately the size of the SNeuPI ionization chamber, shown in Figure 4.8. This box is placed on an insulated surface in the vacuum chamber, which is initially pumped down to the 10^{-7} Torr range. The emitter and MCP are powered by bench power supplies, which are manually adjusted to provide the desired MCP bias and electron emission current. The electron emission current is collected from the walls of the closed proxy box and monitored with a Keithley model 6517B electrometer connected in series with the test setup ground. The MCP output current I_{MCP} is monitored through a Keithley model 6517A electrometer connected in series with the test setup ground; this instrument is connected via GPIB to the LabVIEW control VI, which records I_{MCP} measurements to an output file once per second.

The Anelva ionization gauge controller sends ambient vacuum chamber pressure measurements from the Bayard-Alpert gauge once per second to the control VI, which records the data to an output file. The ambient chamber pressure and accommodation chamber pressure can safely be assumed to be at equilibrium, as the proxy box is not precision machined and closes only tightly enough that most electron emission current can reasonably be assumed to flow to its walls.

The vacuum chamber leak valve is manually opened in small increments to raise the chamber pressure. Measurements are recorded over a dwell time of approximately 10 s per pressure setting, swept from the base pressure up to the low 10^{-5} Torr range. The leak valve is then manually closed in small increments, and pressure data is recorded over a sweep back down

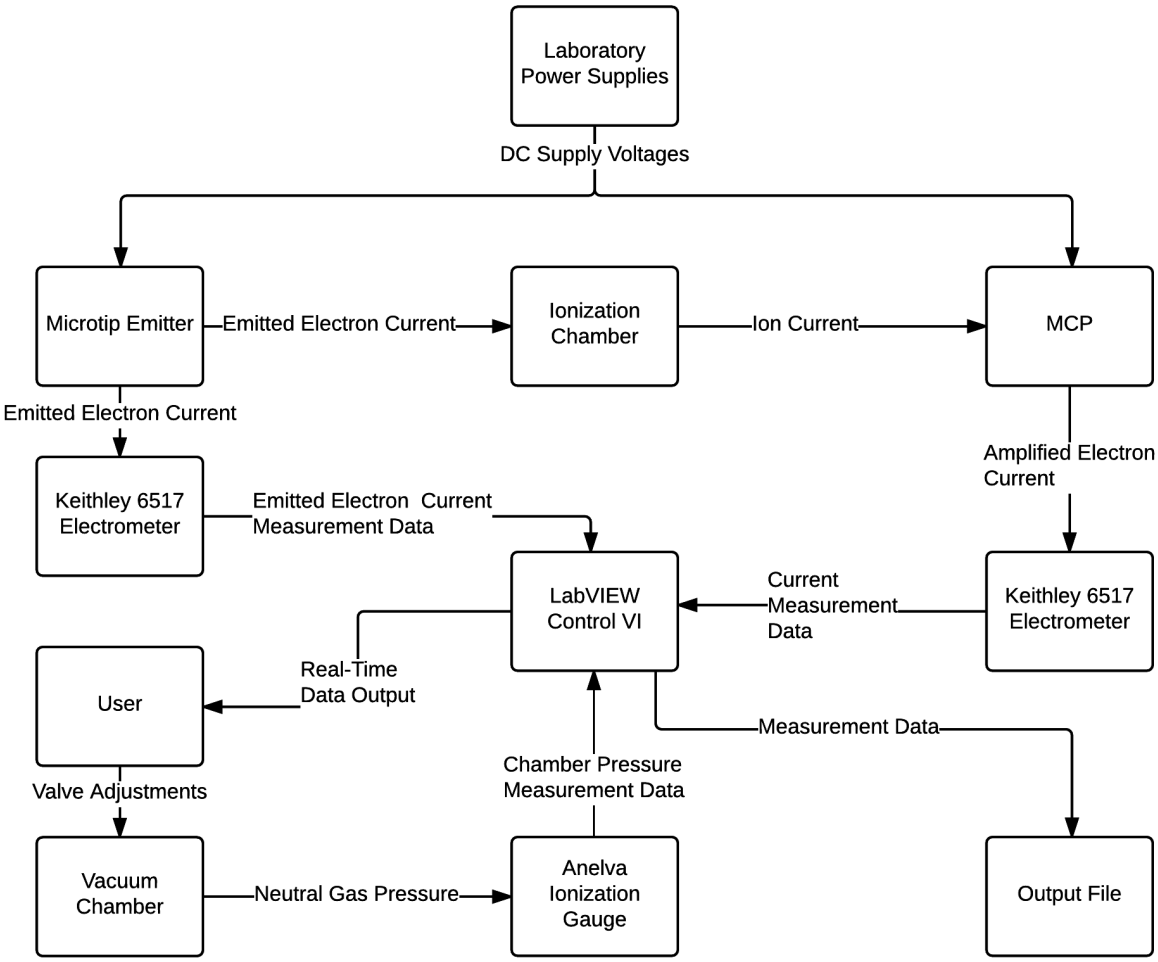

Figure 4.7: Vacuum chamber pressure calibration functional block diagram showing flow of data and control.

to the 10^{-7} Torr range.

4.3.2 Logarithmic Conformance Test Procedure

Logarithmic conformance and temperature calibration data are gathered simulatenously. All three SNeuPI PCBs are powered during the collection of these data; although the SNeuPI emitter control cicuitry is not necessary to conduct a test of the electrometer circuit, it is connected to the FPGA board in the flight configuration. The motivation for including this circuit in the test setup is to account for any EMI noise introduced by the circuit. The block diagram in Figure 4.9 depicts the flow of control and data signals for both the logarithmic conformance and temperature compensation tests.

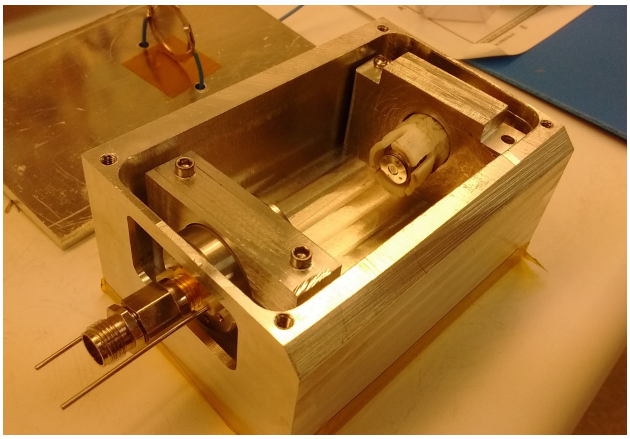

Figure 4.8: Pressure calibration proxy box.

Two external bench power supplies provide DC supply voltages to the SNeuPI boards in lieu of the LIIB board, which will distribute power to SNeuPI in flight. The power supplies are connected to the FPGA board, which distributes the necessary DC voltages to the emitter control and electrometer boards via board interconnect wiring harnesses.

The output of a GPIB-connected PCS is connected to the input Winchester connector of the electrometer circuit. In order to bypass the FPGA board analog signal chain and digital circuitry and directly measure the output of the electrometer circuit, the VI interfaces via GPIB with a Keithley model 6517B electrometer set to function as a voltmeter. The triaxial shielded test lead of this instrument is connected to a test point on the electrometer PCB. This setup enables continuous monitoring of the electrometer's analog output voltage V_{D_DATA}, which the VI samples and records once per second over the duration of the input current sweep. Thus, a total of six output voltage measurement samples are recorded for each distinct PCS test current value.

4.3.3 Temperature Calibration Procedure

In order to develop a temperature compensation algorithm for processing instrument data, circuit performance must be characterized across SNeuPI's expected operating temperature range. Because the Space@VT laboratory lacks the equipment necessary to cool the electrometer circuit while keeping it connected to power and test leads and providing adequate EMI shielding, measurements can only be made at room temperature and above. The performance of the circuit will be extrapolated in order to predict its performance at lower temperatures, and these extrapolations will be compared to low-temperature data obtained during thermal vacuum testing at the University of Illinois. The details of the test data extrapolation procedure are discussed in Section 5.5.

Temperature compensation curves are generated by plotting measured V_{ADC} voltages as a function of test current at different operating temperatures. As described in Section 4.3.2, the PCS outputs each test current value for a total of six seconds over the combined upward

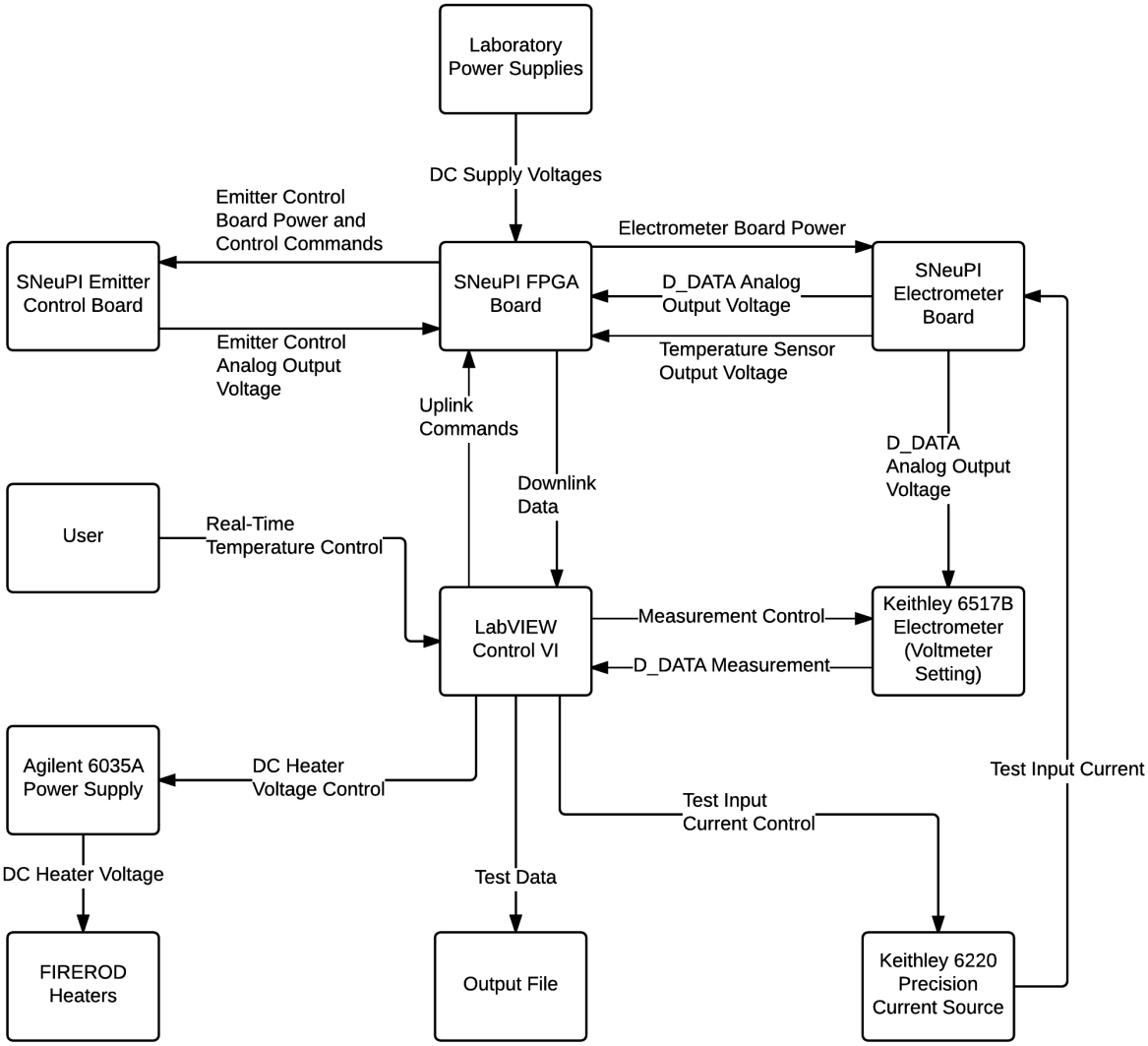

Figure 4.9: Logarithmic conformance/temperature calibration measurement functional block diagram indicating flow of control and data.

and downward test current sweeps. The SNeuPI FPGA board circuitry samples the ADC input voltage representing the MCP current I_{MCP} three times per second, such that a total of eighteen current measurement samples are recorded for each distinct PCS test current value.

In order to vary the circuit operating temperature, the voltage and current to the FIREROD™ heaters are varied. The user monitors the circuit temperature data output by the LTC2997 temperature sensor via the control VI front panel, and manually adjusts the output of the Agilent 6035A power supply as needed to increase or decrease the circuit temperature. Once

a target temperature is reached, the user attempts to adjust the heater supply voltage as necessary in order to maintain the target temperature within an error of no more than ±2 °C for a dwell time of 5 min prior to initiating the test current sweep. This practice is assumed to improve the probability that the different components of the electrometer circuit will reach thermal equilibrium.

Figure 4.10 shows temperature sensor measurements over time for a case in which the circuit is heated from room temperature to a target temperature of 60 °C. The target temperature is reached after about 7.5 min, and held within ±2 °C of the target temperature for over 10 min. The data do appear to trend upward slightly toward the end of the dataset, reaching a peak temperature of about 61.1 °C, but this is likely a result of the imprecise nature of the manual temperature control scheme. Based upon these data, a 5 min dwell time appears more than sufficient to stabilize the circuit temperature.

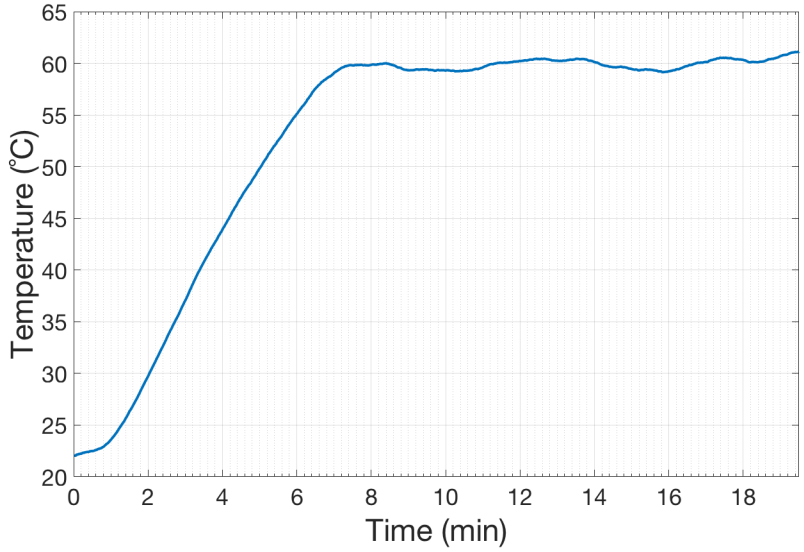

Figure 4.10: Electrometer board temperature sensor measurements vs. time for a case in which the circuit is heated from room temperature to a target temperature of 60 °C. The temperature data are sampled once per second and smoothed using a 30-point moving average scheme to remove high frequency noise.

The target temperatures for temperature compensation curves are room temperature (with no voltage supplied to the FIRERODs™), 35 °C, 45 °C, 55 °C, 60 °C, 65 °C, 70 °C, and 75 °C.

4.3.4 Power Consumption Measurement Procedure

In order to measure the power consumption of the Rev. 1 and Rev. 2 electrometer circuits, Keithley 6517 electrometers are connected to one circuit at a time in series with the required external ±5 V DC power supplies. No other SNeuPI PCBs are powered during this test. Due to the deviation in the Rev. 1 circuit from its expected performance (see Section 2.4), the

power consumption of the current inverter section of this circuit will be measured separately from that of the logarithmic amplifier section of the circuit. The two circuit sections have been isolated on two separate prototype PCBs. Figure 4.11 shows a functional block diagram depicting the flow of data and control for this test.

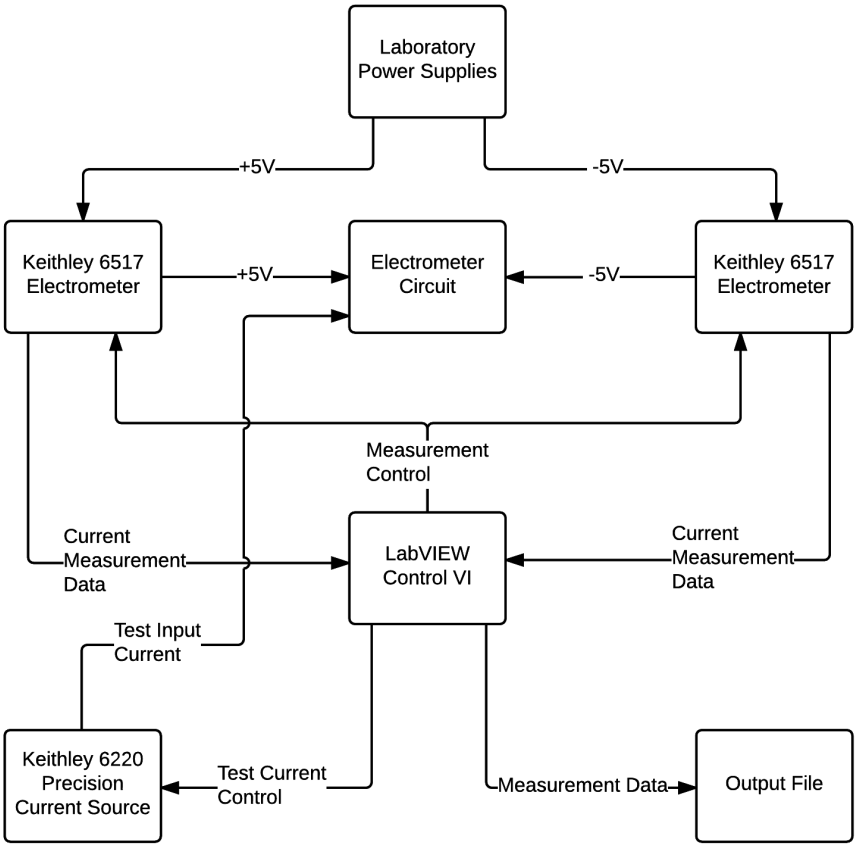

Figure 4.11: Power consumption measurement functional block diagram indicating flow of control and data.

The resultant power consumption data are analyzed to determine the average and maximum power consumption of each revision of the SNeuPI electrometer over the specified input current range.

4.4 Measurement Instrument Calibration

Noel (2015) describes spot-checks of the Space@VT test instrumentation performed in testing the SNeuPI RPA instrument. The present work is carried out under the assumption that these calibration checks are still valid. One factor worthy of note is the variability in accuracy of the Keithley PCS. Table 4.1 depicts noise and accuracy data from the instrument datasheet. Of particular interest to the present work is the fact that the instrument's offset error is

Table 4.1: Keithley 6220 Precision Current Source accuracy and noise. Specifications are at 23 °C ± 5 °C (Keithley Instruments, Inc., 2008)

Range (+5% over range)	**Accuracy ±(% rdg. + A)**	**Programming Resolution**	**Typical Noise (peak–peak/RMS) 0.1Hz–10Hz**	**Typical Noise (peak–peak/RMS) 10Hz–(bw)**
2 nA	0.4% + 2 pA	100 fA	400/80 fA	250/50 pA
20 nA	0.3% + 10 pA	1 pA	4/0.8 pA	250/50 pA
200 nA	0.3% + 100 pA	10 pA	20/4 pA	2.5/0.5 nA
2 µA	0.1% + 1 nA	100 pA	200/40 pA	25/50 nA
20 µA	0.05% + 10 nA	1 nA	2/0.4 nA	500/100 nA

constant over each output current range; the percent error of the output current is therefore theoretically roughly an order of magnitude higher at the lowest output current of each range than at the highest output current of that range. This may prove to be worthy of consideration in analyzing test results.

Chapter 5

Results and Analysis

5.1 Pressure Calibration Results

Results of the vacuum chamber pressure calibration test are shown in Figure 5.1. In order to reduce the effects of outliers, the least squares linear best-fit lines are calculated using bisquare weighting (NIST/SEMATECH, 2016). The calculated best-fit equations are:

$$I_{MCP,112\,\mu A} = 3.267 \times 10^{-2} \times P_{112\,\mu A} + 6.275 \times 10^{-9}; \tag{5.1}$$

$$I_{MCP,131\,\mu A} = 3.837 \times 10^{-2} \times P_{131\,\mu A} + 1.298 \times 10^{-8}; \tag{5.2}$$

$$I_{MCP,150\,\mu A} = 4.176 \times 10^{-2} \times P_{150\,\mu A} + 1.603 \times 10^{-8}. \tag{5.3}$$

In order to enable the conversion from current to pressure measurements, it is useful to rearrange these equations:

$$P_{112\,\mu A} = \frac{I_{MCP,112\,\mu A} - 6.275 \times 10^{-9}}{3.267 \times 10^{-2}}; \tag{5.4}$$

$$P_{131\,\mu A} = \frac{I_{MCP,131\,\mu A} - 1.298 \times 10^{-8}}{3.837 \times 10^{-2}}; \tag{5.5}$$

$$P_{150\,\mu A} = \frac{I_{MCP,150\,\mu A} - 1.603 \times 10^{-8}}{4.176 \times 10^{-2}}. \tag{5.6}$$

These relationships between I_{MCP} and ionization chamber pressure differ somewhat from the expected behavior. One might reasonably make the assumption that, for a neutral gas

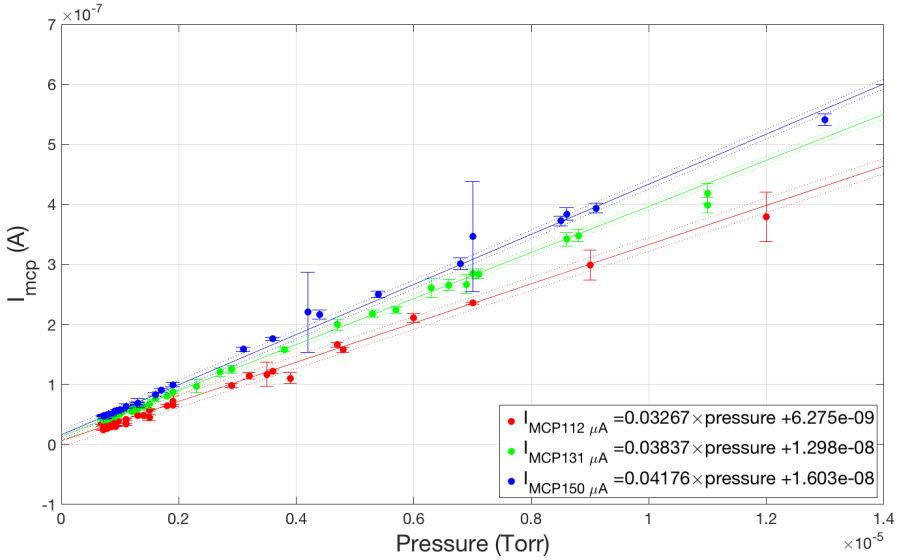

Figure 5.1: Measured pressure calibration data at three electron emission currents. Each point is an average of 2–20 measured I_{MCP} values, with error bar magnitudes equal to two standard deviations of the data at that point. Best-fit lines and 95% confidence intervals are calculated using the linear least squares method with bisquare weighting.

pressure of zero, the MCP would produce zero output current, as no ions would be present to impinge upon the front plate of the device. A significant number of electrons emitted by the Spindt cathode would need to be energetic enough to overcome the −1.5 kV bias of the plate in order to generate a measurable current–a seemingly unlikely scenario. A case can be made for forcing the best-fit lines of the pressure calibration datasets to pass through the plot origin on this basis. However, the fact that the y-axis crossings of the I_{MCP} vs. pressure best-fit lines appear to increase with emission current suggests that either some quiescent MCP current positively correlated with microtip emission current is present, or the I_{MCP} to pressure relationship becomes nonlinear at some pressure below the tested range. The best-fit equations with nonzero I_{MCP} offsets will therefore be used as calculated. It is worth noting that if the apparent quiescent currents do exist, it is not possible for the electrometer circuit to operate over the 100 pA–1 nA decade.

5.2 Expected I_{MCP} Calculation

In order to predict the in-flight performance of the SNeuPI electrometer, it is useful to determine a probable range for I_{MCP} over the duration of the LAICE mission. Circuit performance over this expected range can then be examined under varying operating temperature and ambient pressure conditions. Neutral density data from the MSIS E-90 Atmosphere Model can be used to estimate an operating range of neutral pressures from which an I_{MCP} range

can be calculated (MSIS, 2016). The lowest ambient pressure for the LAICE mission is assumed to occur during the winter solstice at a local time of midnight, an altitude of 450 km, a latitude of 51.6°, and a longitude of 80.4° W. The highest ambient pressure is assumed to occur over the equator during equinox at a local time of noon, an altitude of 200 km, and a longitude of 80.4° W.

According to Hanson et al. (1992), for neutral gas entering a chamber through a small ram-facing aperture on a spacecraft,

$$P_c \approx \sqrt{\pi} n_0 m V v_g, \tag{5.7}$$

where P_c is chamber pressure, n_0 is ambient neutral density, m is the mass of a neutral gas molecule, V is the speed of the spacecraft relative to the ambient gas, and v_g is the most probable velocity of particles inside the chamber. Monatomic oxygen is the dominant constituent of neutral gas over the expected altitude range for the LAICE mission.

In order to calculate a worst-case low value of I_{MCP}, a chamber neutral gas temperature of $-20\,^{\circ}\mathrm{C} = 253.15\,\mathrm{K}$ is assumed, corresponding with the lower limit of the specified operating temperature range for SNeuPI.

The most probable particle velocity is

$$v_g = \sqrt{\frac{2kT}{m}}, \tag{5.8}$$

where k is Boltzmann's constant:

$$k = 1.3806 \times 10^{-23}\,\mathrm{J\,K^{-1}}. \tag{5.9}$$

The mass of an oxygen atom in kilograms is

$$m = 2.6568 \times 10^{-26}\,\mathrm{kg}. \tag{5.10}$$

Substituting the results from Equations 5.9 and 5.10 into Equation 5.8 yields

$$v_g = 513.01\,\mathrm{m\,s^{-1}} \tag{5.11}$$

According to MSIS (2016), on December 23, 2015, at 12:00 AM local time, 51.6° latitude, 80.4° W longitude and 450 km altitude,

$$n_0 = 2.59 \times 10^{7}\,\mathrm{cm^{-3}} = 2.59 \times 10^{13}\,\mathrm{m^{-3}}. \tag{5.12}$$

For an altitude of 450 km, the orbital velocity is

$$V = 7643\,\mathrm{m\,s^{-1}}. \tag{5.13}$$

Substituting Equations 5.10, 5.11, 5.12, and 5.13 into Equation 5.7 yields

$$P_c = 4.782\,\mu\mathrm{Pa} = 35.87\,\mathrm{nTorr}. \tag{5.14}$$

Substituting the result of Equation 5.14 into Equation 5.1 yields

$$I_{MCP,min} = 7.45\,\mathrm{nA} \tag{5.15}$$

for a microtip emission current of 112 µA.

According to MSIS (2016), on March 20, 2015, at 12:00 PM local time, 0° latitude, 80.4° W longitude and 200 km altitude,

$$n_0 = 8.98 \times 10^9\,\mathrm{cm^{-3}} = 8.98 \times 10^{15}\,\mathrm{m^{-3}}. \tag{5.16}$$

For an altitude of 200 km, the orbital velocity is

$$V = 7787\,\mathrm{m\,s^{-1}}. \tag{5.17}$$

Assuming a neutral gas temperature inside the accommodation chamber to be 75 °C=348.15 K, Equation 5.11 evaluates as

$$v_g = 601.53\,\mathrm{m\,s^{-1}}. \tag{5.18}$$

Reevaluating Equation 5.7 yields

$$P_c = 1.981\,\mathrm{mPa} = 14.86\,\mu\mathrm{Torr}. \tag{5.19}$$

Substituting the result of Equation 5.19 into Equation 5.3 yields

$$I_{MCP,max} = 636.5\,\mathrm{nA}. \tag{5.20}$$

These results and calculation results for similar conditions assuming an accommodated neutral gas temperature of 300 K are summarized in Table 5.1.

Table 5.1: Sample MSIS neutral density data and corresponding calculated chamber pressure and I_{MCP} (MSIS, 2016).

Date	**Local Time**	**Latitude**	**Altitude (km)**	n_0 ($\mathbf{m}^{-3}$)	**T (K)**	P_c (Torr)	**Calculated I_{MCP} (A)**		
							$I_{emiss} = 112\,\mu A$	$I_{emiss} = 131\,\mu A$	$I_{emiss} = 150\,\mu A$
12/23/15	12:00 AM	51.6°	450	2.59×10^{13}	253.15	3.59×10^{-8}	7.45×10^{-9}	1.44×10^{-8}	1.75×10^{-8}
12/23/15	12:00 AM	51.6°	450	2.59×10^{13}	300.00	3.90×10^{-8}	7.55×10^{-9}	1.45×10^{-8}	1.77×10^{-8}
3/20/15	12:00 PM	0°	200	8.98×10^{15}	300.00	1.38×10^{-5}	4.57×10^{-7}	5.42×10^{-7}	5.92×10^{-7}
3/20/15	12:00 PM	0°	200	8.98×10^{15}	348.15	1.49×10^{-5}	4.92×10^{-7}	5.83×10^{-07}	6.36×10^{-7}

5.3 Logarithmic Conformance Validation

Figure 5.2 shows the plotted results of the logarithmic conformance test at room temperature, as well as the best-fit line for the data. This and all other nonlinear best-fit curves presented in this paper are calculated in MATLAB using a Levenberg-Marquardt algorithm (Marquardt, 1963). The best-fit equation of the logarithmic conformance test results is

$$V_{D\_DATA}(V) = 0.3813 \times \ln\left(I_{MCP}(A)\right) + 6.585. \tag{5.21}$$

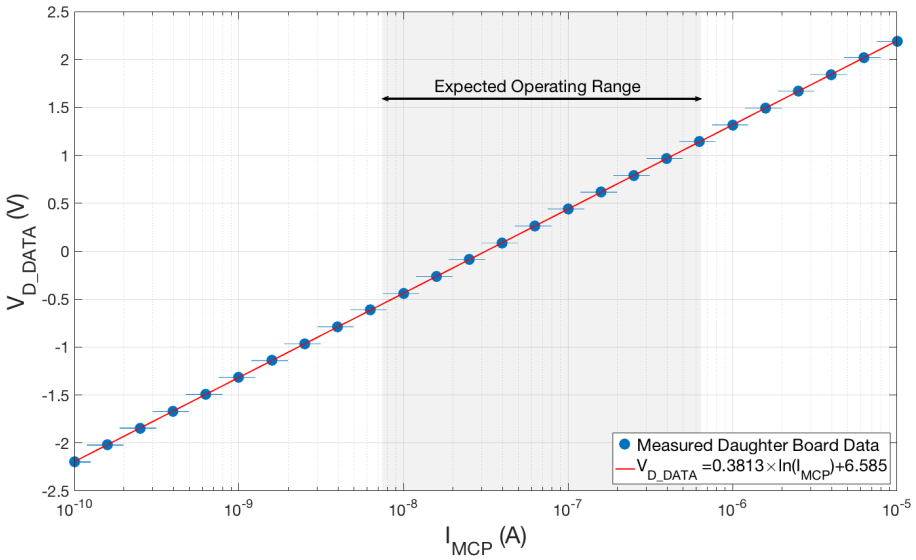

Figure 5.2: Measured response of the Rev. 2 SNeuPI electrometer circuit pre-conformal coating. Error bar magnitudes are two standard deviations of each V_{D_DATA} data point; note that error bar magnitudes are so small that only handles are visible. The best-fit line as calculated by MATLAB is shown in red.

A high degree of logarithmic conformance is evident by visual inspection of the plot. The percent error of each data point as compared to the best-fit logarithmic function can be

calculated as follows:

$$\%error = 100 \times \left| \frac{V_{meas} - V_{fit}}{V_{fit}} \right|, \tag{5.22}$$

where V_{meas} is the measured value of V_{D_DATA} at a given data point and V_{fit} is the value of V_{D_DATA} predicted by the best-fit equation for the value of I_{MCP} at that data point. Performing this calculation for each measured data point yields the data shown in Figure 5.3. The error is less than 2% across the operating range, with a worst-case error of about 1.07% for an I_{MCP} value of 25.1 nA. The cause of the pronounced peak in the percent error at this value of MCP current is uncertain. However, it is worth noting that this data point occurs at the low end of one of the output ranges of the Keithley PCS used to perform the test, as shown in Table 4.1. That the percent error peaks at this point and appears to smoothly fall off over the next decade of test current values suggests that the constant offset current error of the PCS at this range may be more significant than at other ranges.

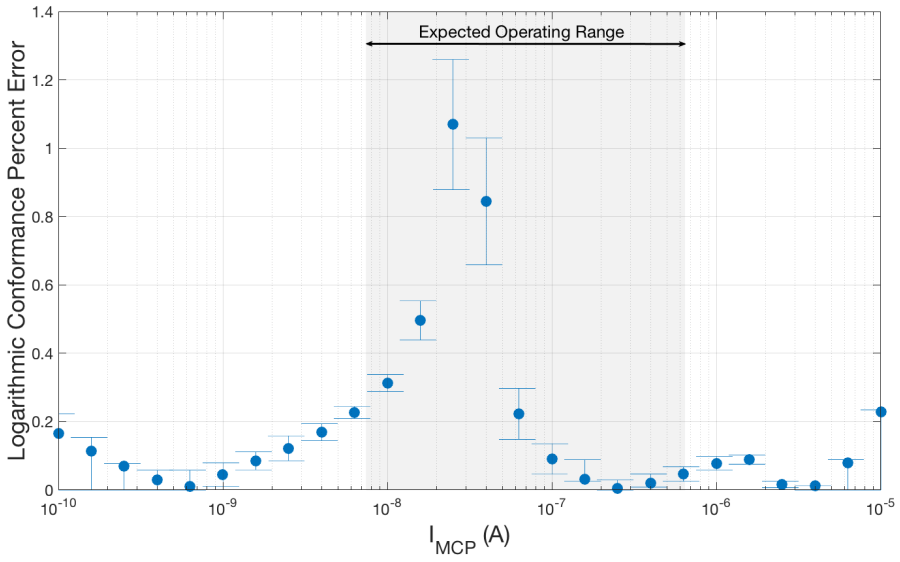

Figure 5.3: Logarithmic conformance percent error as a function of electrometer input current I_{MCP}. Error bar magnitude at each point corresponds to a variability in sampled V_{ADC} value of two standard deviations. Note that the error is less than 2% across the entire operating range.

5.4 Temperature Calibration Data

The goal of the electrometer circuit temperature compensation algorithm is to empirically derive a formula for I_{MCP} as a function of both V_{ADC} and operating temperature. Therefore, although I_{MCP} is actually the independent variable of the temperature calibration tests, the results will be presented in the form of I_{MCP} vs. V_{ADC} plots. Best-fit lines calculated

in MATLAB using the Levenberg-Marquardt fitting algorithm are plotted along with the measured data. Calibration curves at three different temperatures are shown in Figures 5.4–5.6. Additional temperature calibration plots are shown in Appendix A.

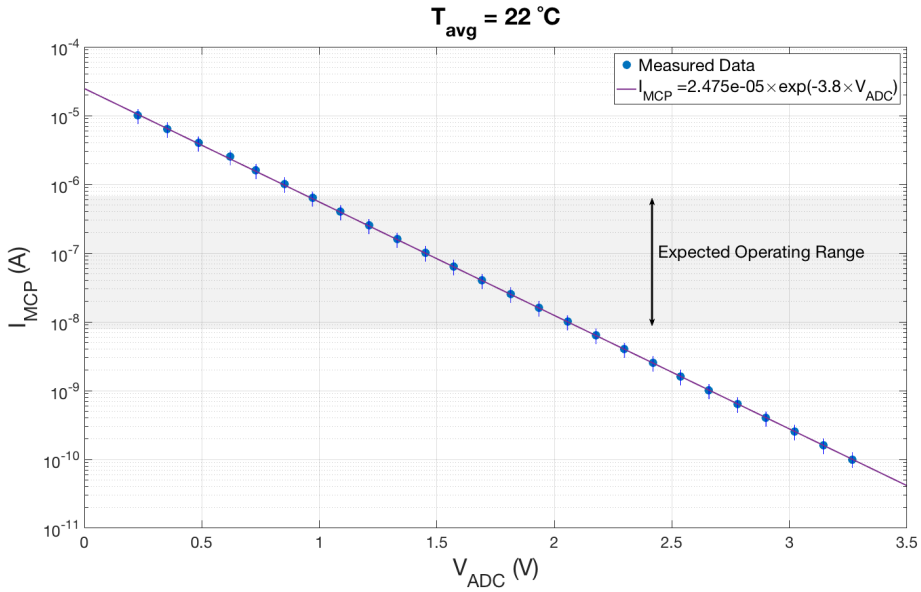

Figure 5.4: Room temperature calibration curve; mean temperature over current sweep is 22 °C. Error bar magnitudes are equal to two standard deviations of each V_{ADC} data point; note that error bar magnitudes are so small that only handles are visible. The best-fit line as calculated by MATLAB is shown in purple, and the range of expected operating input currents is shaded.

For circuit operating temperatures of 60 °C and higher, deviations in the I_{MCP} vs. V_{ADC} relationship from the best-fit exponential curves begin to manifest at the low end of the current range, as shown in Figures 5.5 and 5.6. The estimates presented in Section 5.2 suggest that the electrometer circuit will most likely not operate at this range of input currents in flight. For each dataset in this temperature range, datapoints in this region deviating sigificantly from the expected exponential behavior are excluded in the calculation of the best-fit curve in order to optimize the fit to the operational region of the dataset. This decision is made at the expense of greater error in prediction of temperature-dependent circuit behavior in these deviant operational regions. Some further discussion of this deviant behavior is worthwhile.

Two likely causes of these deviations at the top end of the operating temperature range are input transistor reverse saturation current I_S and input-stage op amp bias current I_{bias}.

In Equation 3.4, the assumption was made that I_{MCP} is much larger than I_S of the input stage transistors. The mathematical relationship between I_S and temperature is difficult to determine, but one might reasonably suspect that large variations in operational temperature could alter the magnitude of this parameter enough to cause visible deviations in circuit performance. For cases in which I_S is comparable in magnitude to I_{MCP}, the I_{MCP} vs. V_{ADC}

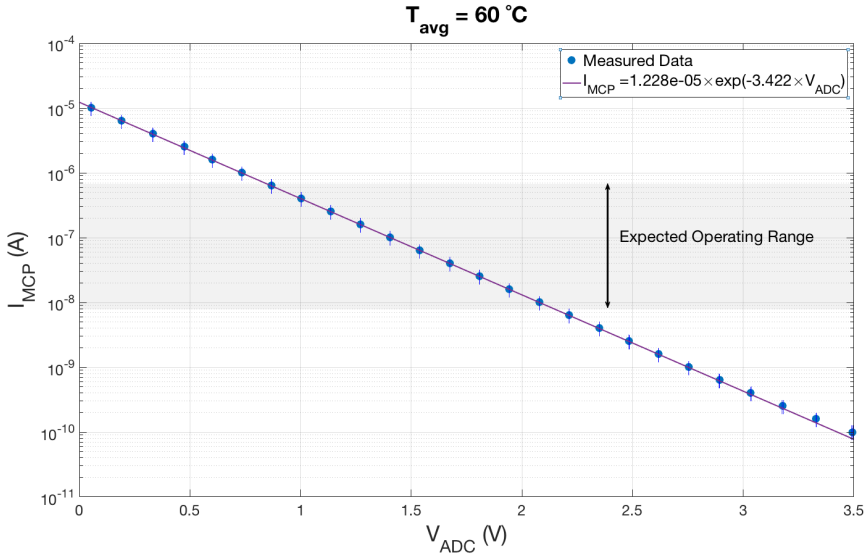

(a)

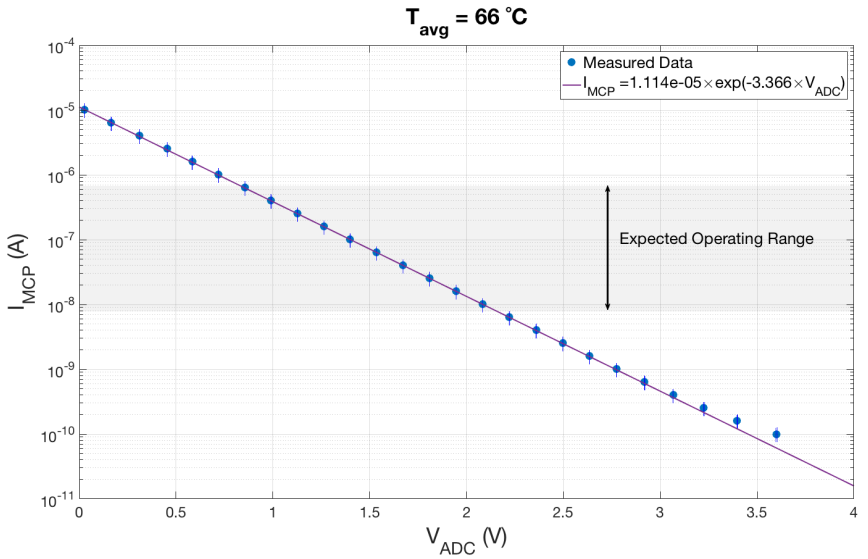

(b)

Figure 5.5: Calibration curves for mean temperatures 60 °C (a) and 66 °C (b). Error bar magnitudes are equal to two standard deviations of each measured V_{ADC} data point; note that error bar magnitudes are so small that only handles are visible. Also note that slight deviation from logarithmic conformance is visible over the data points corresponding to the lowest 3–4 test currents. The best-fit lines as calculated by MATLAB are shown in purple, and the range of expected operating input currents is shaded.

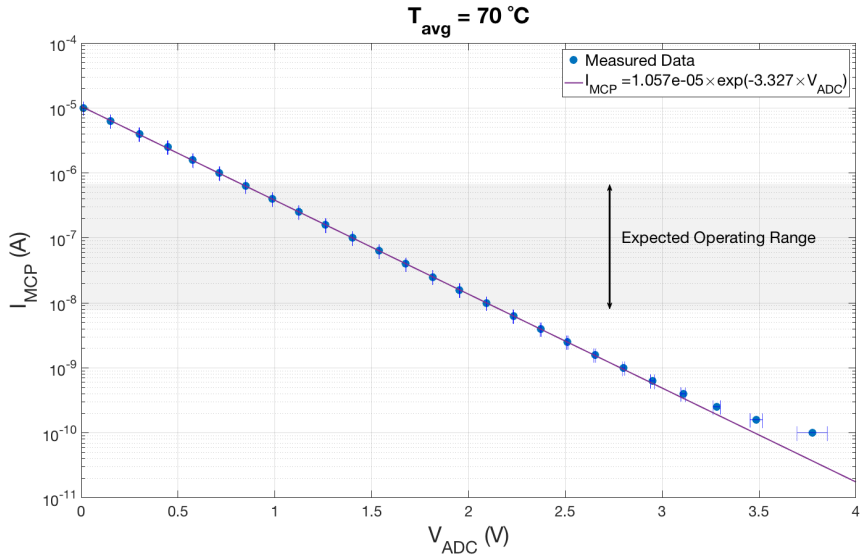

(a)

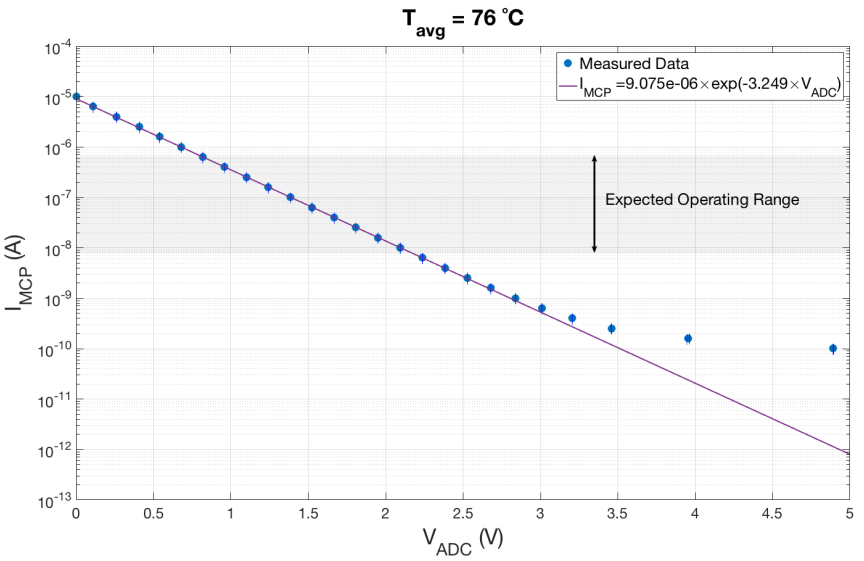

(b)

Figure 5.6: Calibration curves for mean temperatures 70 °C (a) and 76 °C (b). Error bar magnitudes are equal to two standard deviations of each measured V_{ADC} data point. Note that significant deviation from logarithmic conformance is visible over the data points corresponding to the lowest 3–4 test currents. The best-fit lines as calculated by MATLAB are shown in purple, and the range of expected operating input currents is shaded.

relationship becomes

$$I_{MCP} = I_S \left[exp\left(\frac{\frac{370V_{ADC}}{255} - 2.5}{-\left(\frac{100}{101.5}\right)\left(1+\frac{50}{3.57}\right)V_T} \right) \left(\frac{I_{ref}}{I_S} + 1 \right) - 1 \right]. \tag{5.23}$$

The relationships between I_S and I_{bias} and temperature are unknown. Figure 5.7 depicts modeled circuit responses for four cases: the ideal case neglecting the effects of I_S and I_{bias}, a case neglecting I_S but with I_{bias}=100 pA flowing into the inputs of the logarithmic amplifier stage op amps, a case neglecting I_S but with I_{bias}=100 pA flowing out of the op amp inputs, and a case neglecting I_{bias} but with I_S=100 pA.

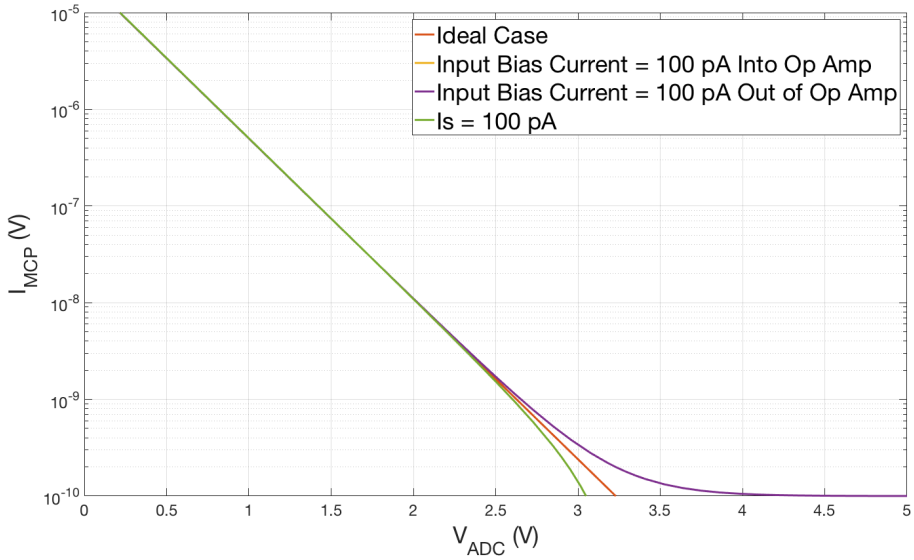

Figure 5.7: Modeled I_{MCP} vs. V_{ADC} response curves showing the effects of I_S and I_{bias}. 100 pA I_S and 100 pA I_{bias} flowing into the op amp have the same effect and cannot be visually distinguished in the plot. 100 pA flowing out of the op amp has a similar effect as observed in the measured data at 76 °C (see Figure 5.6b). Model temperature is 25 °C.

The effects of I_S and I_{bias} flowing into the op amp have the same effect: the I_{MCP} vs. V_{ADC} response begins to noticeably deviate from the ideal response at $V_{ADC} \approx 2.25$ V, with the value of I_{MCP} dropping more rapidly than the ideal response for increasing V_{ADC}. The effect of I_{bias} flowing out of the op amp, however, closely resembles the temperature calibration data measured at an operating temperature of about 76 °C. As V_{ADC} approaches 5 V, I_{MCP} asymptotically approaches 100 pA.

This effect is due to I_{MCP} being entirely sourced by the bias current of the input stage logarithmic amplifier op amp, as shown in Figure 5.8. In this case, no current flows through the feedback diode, and the output voltage of the logarithmic amplifier is 0 V. The output of

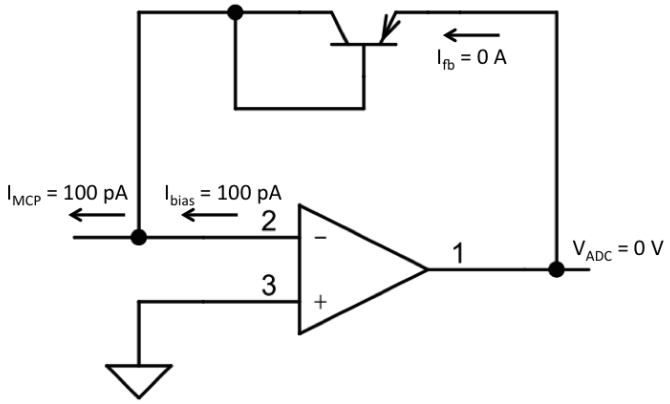

Figure 5.8: A logarithmic amplifier stage showing the effect of high bias current flowing out of the op amp.

the following differential amplifier stage therefore saturates at −5 V. This voltage is passed through the unity gain inverting amplifier, the 2.5 V offset summing amplifier, and the ADC protection voltage divider, resulting in a V_{ADC} voltage of approximately 5 V. The similarity of this modeled behavior to the measured circuit performance at the top end of the temperature range suggests that the observed deviations from the ideal response are likely a result of increased input stage bias current. This raises suspicions that the LMC6482 op amp bias current may be more susceptible to temperature effects than indicated by its datasheet (Texas Instruments Incorporated, 2015).

5.5 Temperature Compensation Algorithm

The next step in determining the temperature-dependent behavior of the electrometer circuit is to analyze the collected temperature calibration data for meaningful trends. Figure 5.9 shows a flowchart of the algorithm for gathering and analyzing temperature data for the electrometer circuit.

In order to experimentally determine the temperature dependencies of the $c\,(T_C)$ and $d\,(T_C)$ terms of the inverse transfer function given in Equation 3.29, these terms are extracted from the best-fit equation of each temperature calibration datasest of the form presented in Section 5.4 and plotted as a function of the mean recorded circuit temperature for that dataset, as shown in Figures 5.10 and 5.11. Best-fit equations are calculated to fit the forms derived for $c\,(T_C)$ and $d\,(T_C)$ in Section 3.2:

$$c\,(T_C) = a \times exp\left(\frac{b}{T_C + 273.15}\right) \tag{5.24}$$

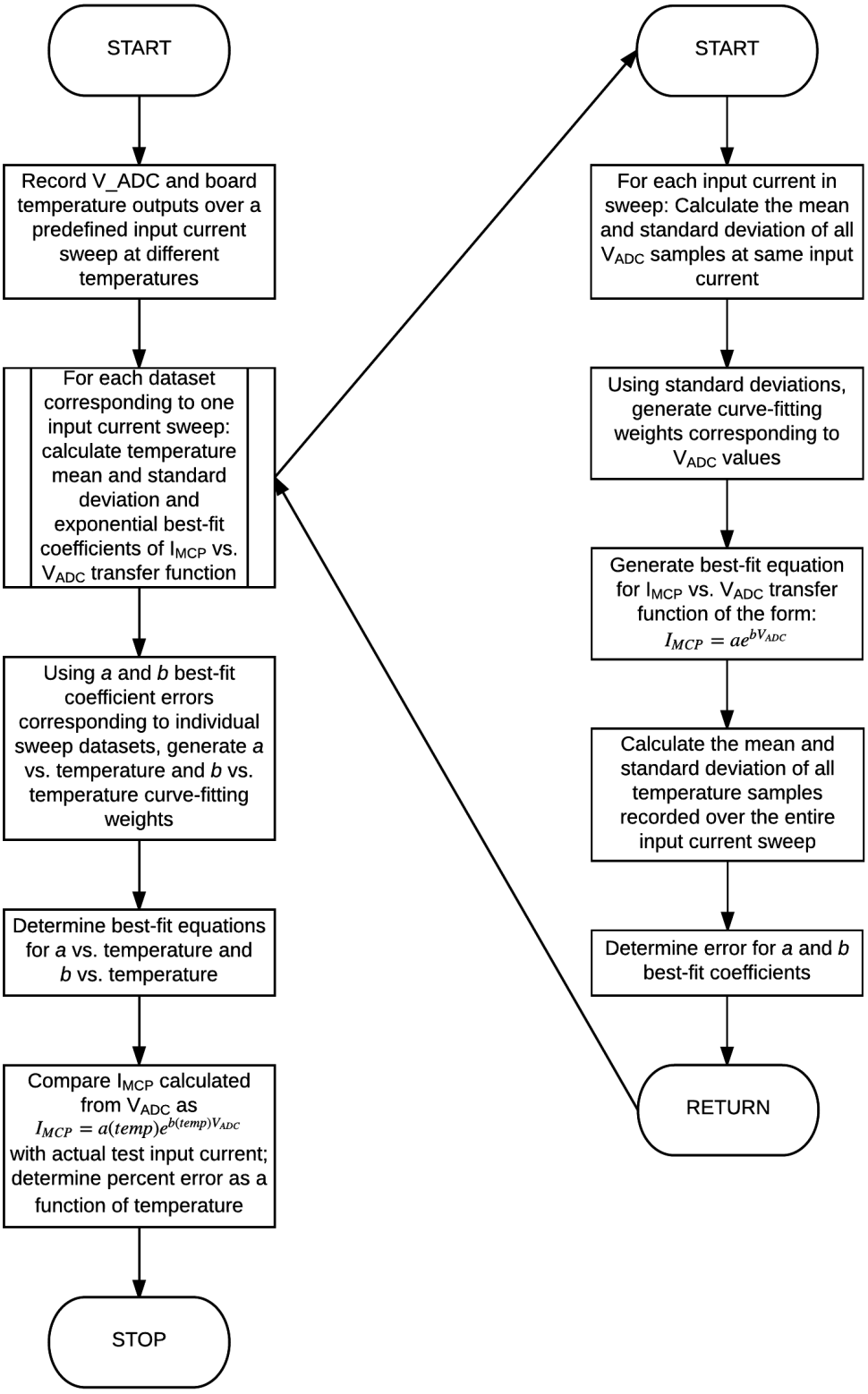

Figure 5.9: Flowchart detailing temperature compensation algorithm.

and

$$d\left(T_C\right) = \frac{u}{T_C + 273.15}. \tag{5.25}$$

The datasets for both $c(T_C)$ and $d(T_C)$, are more closely matched to a third-order polynomial best-fit form than the derived forms shown above. Curves of both theoretical and third-order polynomial forms are shown in Figures 5.10 and 5.11. The case could be made for using the third-order polynomial best-fit equations in processing instrument data. The basis for this argument is that the derived forms of the temperature dependent terms certainly fail to account for various physical unknowns, such as nonidealities in component response, and the superior fit of the third-order form suggests that it may account for these factors. Both best-fit forms are presented in order that the reader may decide for him- or herself which form is more worthy of consideration. The derived forms will be used in the remainder of this document, as their theoretical bases are known. These are:

$$c\left(T_C\right) = 3.279 \times 10^{-8} \times exp\left(\frac{1962}{T_C + 273.15}\right) \tag{5.26}$$

and

$$d\left(T_C\right) = \frac{-1132}{T + 273.15}. \tag{5.27}$$

The resulting temperature-dependent inverse tranfer function is:

$$I_{MCP}(T_C, V_{ADC}) = 3.279 \times 10^{-8} \times exp\left(\frac{1962}{T_C + 273.15}\right) \times exp\left(\frac{-1132 \times V_{ADC}}{T_C + 273.15}\right). \tag{5.28}$$

5.6 Temperature Compensation Results

In order to determine the accuracy of the empirically-derived temperature-dependent transfer function, the ADC voltage and circuit temperature data from the temperature calibration tests are substituted into Equation 5.28. The percent error of the resultant calculated values for I_{MCP} can then be determined based upon the nominal output currents from the Keithley PCS corresponding to each data point. Note that this result will include any error resulting from deviation of the actual PCS output current from the nominal values, as well as any other sources of uncertainty related to the test equipment setup.

Figures 5.12–5.14 show plots of I_{MCP} and pressure measurement percent error as a function of nominal test current at different operating temperatures, and additional plots are shown in Appendix A. For all electrometer input currents above the expected minimum I_{MCP} of 6 nA

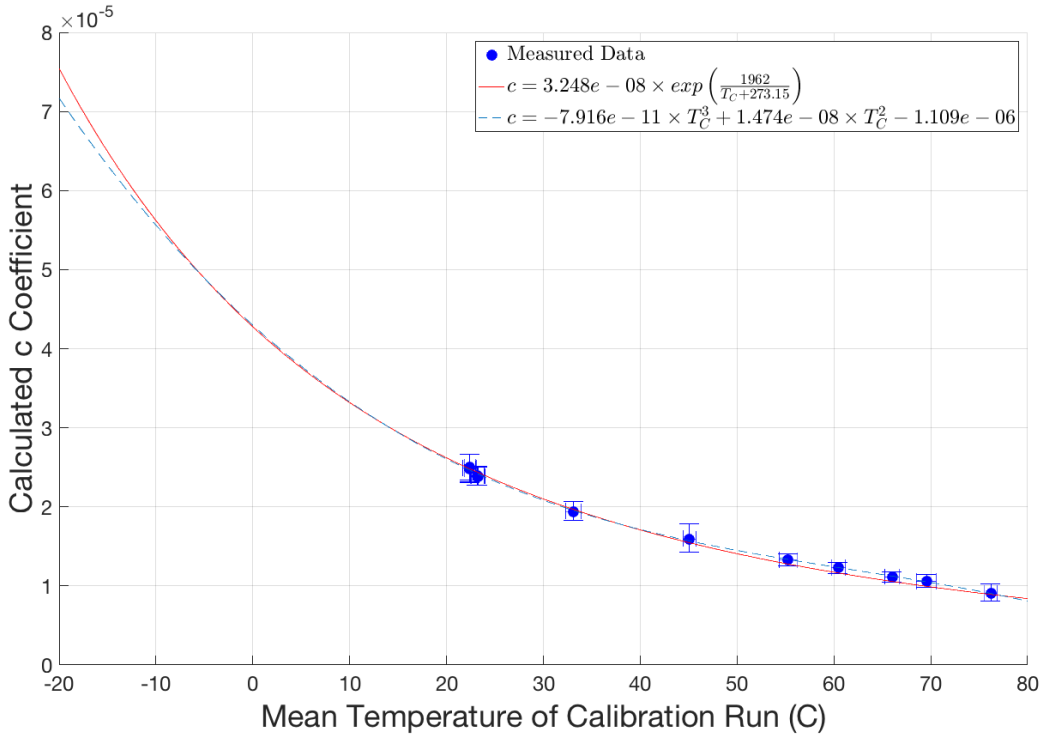

Figure 5.10: I_{MCP} vs. V_{ADC} best-fit coefficient c vs. temperature. The vertical error bar magnitudes are determined by the 95% confidence intervals generated in MATLAB for each $c(T_C)$ value, and the horizontal error bar magnitudes are equal to two standard deviations of the measured temperature of the calibration run producing each point.

and operating temperatures below 60 °C, I_{MCP} percent error is below 6%; pressure percent error at sampled currents is less than 15% for an electron emission current of 112 µA across the expected operating range.

Note that there are fewer data points for pressure percent error than there are for I_{MCP} percent error. This is because test input currents smaller than the constant terms of the pressure calibration equations (Equations 5.1–5.3) correspond to negative pressure values, and therefore have no physical meaning. Due to the linear relationship between I_{MCP} and pressure, the percent errors of the two quantities are approximately the same for cases in which I_{test} is significantly greater in magnitude than the constant terms of the calibration equations. However, for I_{test} values of similar magnitude to the constant terms, the pressure measurement percent error becomes large due to the fact that the electromter circuit's I_{MCP} error approaches a constant percentage of the zero pressure bias current as pressure becomes arbitrarily small. Pressure percent error therefore grows asymptotically as I_{test} approaches these current values.

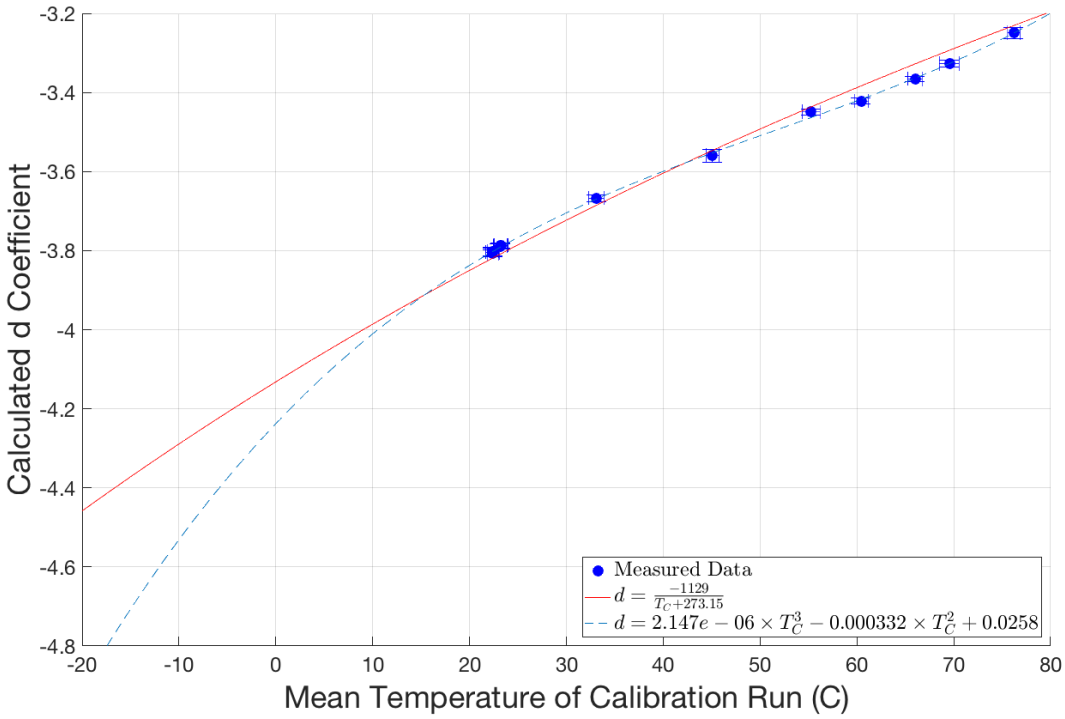

Figure 5.11: I_{MCP} vs. V_{ADC} best-fit coefficient d vs. temperature. The vertical error bar magnitudes are determined by the 95% confidence intervals generated in MATLAB for each $d(T_C)$ value, and the horizontal error bar magnitudes are equal to two standard deviations of the measured temperature of the calibration run producing each point.

A peaking trend in measurement error is evident at a test current of 2.2 µA. This behavior is reminiscent of the peaking of the logarithmic conformance percent error plot in Figure 5.3. As in that case, the peaking in the I_{MCP} measurement percent error plots occurs for currents corresponding to the bottom end of an output range of the PCS. However, the peak in these test data occurs at a test current two decades higher than the previously observed error peak. The cause of this behavior is unknown, but it is worth noting that although data for the logarithmic conformance and the temperature compensation tests are gathered simultaneously, different laboratory instruments are used in collecting the two datasets. Specifically, the logarithmic conformance test uses a Keithley 6517 electrometer set to function as a voltmeter to measure the analog output of the electrometer circuit, while the temperature compensation test data are measured and digitized by the SNeuPI circuitry. These test setup differences may well contribute to the differences in measurement error peaking patterns.

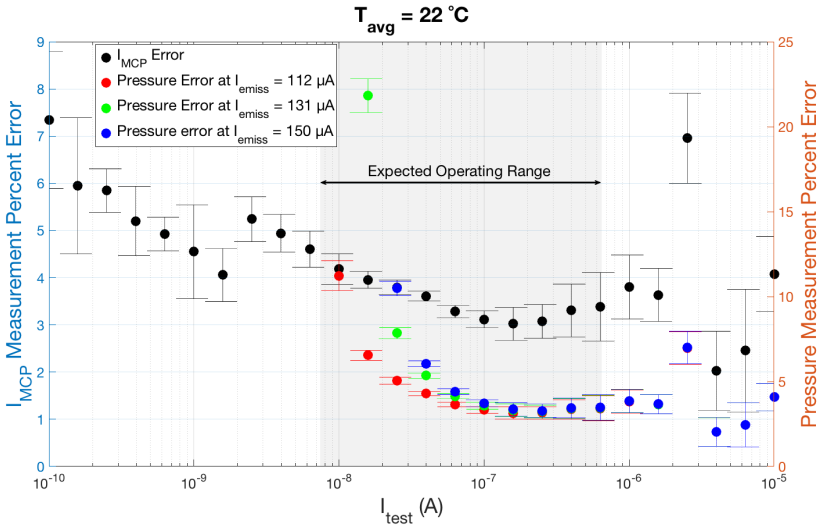

Figure 5.12: Temperature compensated measurement percent error vs. test current at 22 °C. Error bar magnitudes correspond to an I_{MCP} measurement variability of two standard deviations.

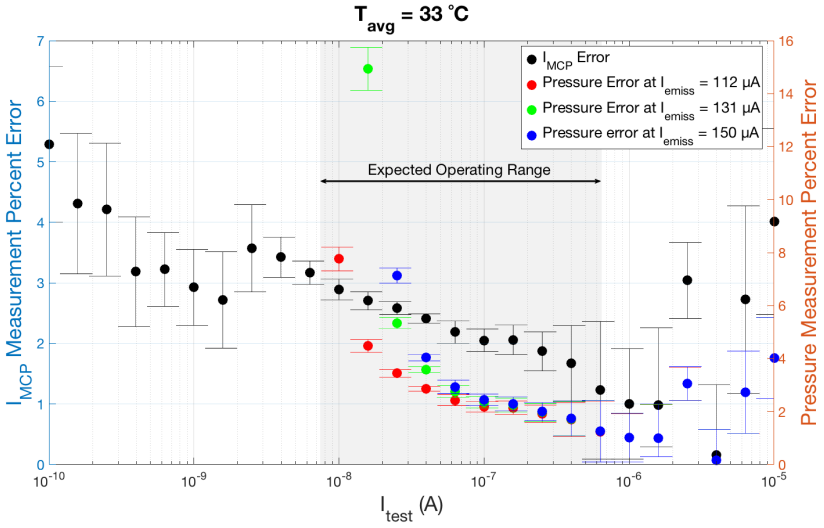

Figure 5.13: Temperature compensated measurement percent error vs. test current at 33 °C. Error bar magnitudes correspond to an I_{MCP} measurement variability of two standard deviations.

5.7 Sensitivity

Sensitivity of the SNeuPI electrometer circuit is limited by the noise of the instrument and its associated analog electronics. The electrometer circuit noise at a given temperature is estimated as the RMS average of the standard deviations of V_{ADC} samples across a full sweep of I_{MCP} test currents. Because test measurements are susceptible to the cumulative noise

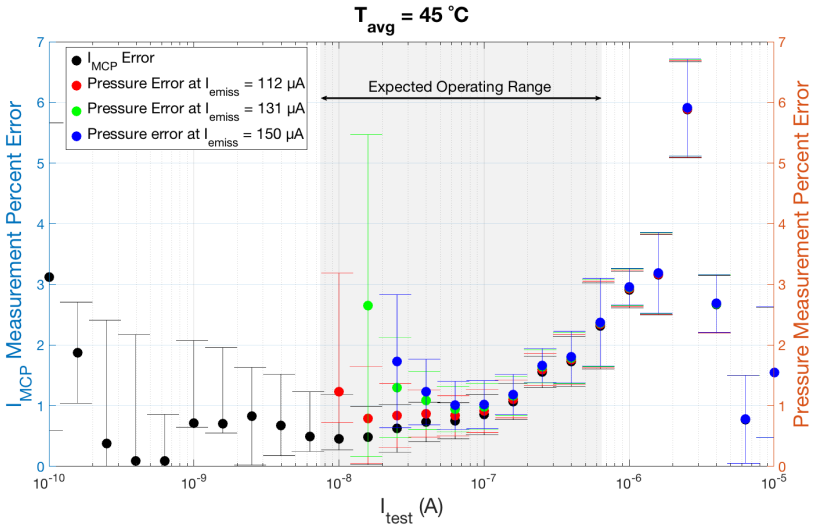

Figure 5.14: Temperature compensated I_{MCP} measurement percent error vs. test current at 45 °C. Error bar magnitudes correspond to an I_{MCP} measurement variability of two standard deviations.

contributions of the test instrumentation, test setup environment, and device under test, this value should be regarded as a worst-case approximation. The actual instrument noise will likely be less than this estimated value.

Because of the exponential relationship between I_{MCP} and V_{ADC}, a constant RMS noise voltage across the entire range of input currents will cause the smallest resolvable input current difference to increase in magnitude as input current magnitude increases. In other words, absolute input current resolution is a function of input current. However, the input current percent sensitivity will be fairly constant across the entire range. The sensitivity-limited percent error in I_{MCP} resulting from RMS noise voltage for a given Celsius temperature T_C and a sampled ADC voltage V_{ADC} can be estimated as

$$\%sens = 100 \times \left| \frac{I_{MCP}(T_C, V_{ADC}) - I_{MCP}(T_C, [V_{ADC} \pm V_{noise}])}{I_{MCP}(T_C, V_{ADC})} \right|, \tag{5.29}$$

where V_{noise} is the measured RMS noise voltage at the operating temperature of interest. The results of this calculation for the SNeuPI electrometer at seven different operating temperatures are summarized in Table 5.2. The measured RMS noise at room temperature is assumed in the calculation for the $T_C = -20\,°\text{C}$ case.

Sensitivity is also limited by the resolution of the ADC. For a power supply voltage of 5 V, the resolution of a 16-bit ADC as used in the SNeuPI design is

$$Res_{ADC} = \frac{5\,\text{V}}{2^{16}} = 76.29\,\mu\text{V}. \tag{5.30}$$

Table 5.2: Electrometer analog noise and noise-limited I_{MCP} percent sensitivity. Because no data were measured at temperatures below 22 °C, the RMS noise observed for the 22 °C case is assumed for calculation of the sensitivity at −20 °C.

Temperature (°C)	**RMS Noise (V)**	**Noise-Limited Sensitivity ($\%I_{MCP}$)**
-20	1.69E-04 (assumed)	$< 7.56 \times 10^{-2}$
22	1.69E-04	$< 6.47 \times 10^{-2}$
33	7.90E-04	$< 2.92 \times 10^{-1}$
45	1.25E-03	$< 4.45 \times 10^{-1}$
55	1.26E-03	$< 4.32 \times 10^{-1}$
66	4.74E-04	$< 1.58 \times 10^{-1}$
76	9.34E-04	$< 3.03 \times 10^{-1}$

Because this value is significantly lower than the calculated RMS noise voltages at different temperatures shown in Table 5.2, analog noise is the dominant factor in determining worst-case instrument sensitivity, and ADC resolution can be ignored.

Letting $P(I_{MCP})$ represent accommodation chamber pressure as a function of I_{MCP} for a given microtip emission current, instrument sensitivity in terms of absolute pressure is

$$sens = \left| P(I_{MCP}) - P\left[I_{MCP} \times \left(1 \pm \frac{\%sens_{Imcp}}{100} \right) \right] \right|. \tag{5.31}$$

Table 5.3 summarizes the results of this calculation for several different pressure values.

Table 5.3: SNeuPI instrument absolute and percent pressure sensitivity data.

P_C **(Torr)**	**Absolute Pressure Sensitivity (Torr)**			**Percent Pressure Sensitivity (%)**		
	$I_{emiss} = 112\,\mu A$	$I_{emiss} = 131\,\mu A$	$I_{emiss} = 150\,\mu A$	$I_{emiss} = 112\,\mu A$	$I_{emiss} = 131\,\mu A$	$I_{emiss} = 150\,\mu A$
3.90×10^{-8}	1.51×10^{-10}	2.44×10^{-10}	2.66×10^{-10}	3.87×10^{-1}	6.26×10^{-1}	6.82×10^{-1}
3.59×10^{-8}	1.49×10^{-10}	2.42×10^{-10}	2.64×10^{-10}	4.15×10^{-1}	6.76×10^{-1}	7.37×10^{-1}
1.38×10^{-5}	9.14×10^{-9}	9.15×10^{-9}	8.92×10^{-9}	6.63×10^{-2}	6.64×10^{-2}	6.47×10^{-2}
1.49×10^{-5}	4.61×10^{-8}	4.61×10^{-8}	4.49×10^{-8}	3.10×10^{-1}	3.10×10^{-1}	3.02×10^{-1}

5.8 Power Consumption Test Results

The results of the power consumption test are shown in Table 5.4. As stated in Chapter 4, the Rev. 1 current inverter is tested separately from the rest of the Rev. 1 electrometer circuit. The LTC2997 temperature sensor is operational during both the Rev. 1 and Rev. 2 electrometer tests, although its output is not loaded. Both electrometer circuits are loaded with a 30 MΩ resistance to ground, as this is the resistance normally seen by the output of the electrometer. The Rev. 2 electrometer consumes less power over the specified input current range of 100 pA–10 µA than the Rev. 1 electrometer without the current inverter circuit. Therefore, although a power consumption analysis has not been performed for the

complete SNeuPI instrument, the stated goal of designing an electrometer with equal or lower power consumption than the Rev. 1 design has been met.

Table 5.4: Average and maximum power consumption test results for the Rev. 1 and Rev. 2 electrometer circuits. Both Rev. 1 and Rev. 2 electrometer circuits are tested with LTC2997 temperature sensor operational but not loaded.

Circuit	$P_{avg}(W)$	$P_{max}(W)$
Rev. 1 Current Inverter	7.78×10^{-4}	4.65×10^{-3}
Rev. 1 Electrometer without Current Inverter	9.02×10^{-2}	9.53×10^{-2}
Rev. 2 Electrometer	6.84×10^{-2}	6.92×10^{-2}

Chapter 6

Conclusions and Outstanding Issues

6.1 Conclusions

The objectives for this work outlined in Chapter 1 have been met. A logarithmic electrometer has been designed and extensively tested, and evaluation of its performance has indicated satisfactory accuracy and sensitivity. The temperature compensation algorithm presented in Section 5.5 will enable reasonably accurate analysis of flight measurement data over the expected operating conditions. Deviations from the expected response of the circuit have been characterized, as have their effects on the accuracy and sensitivity of instrument pressure measurements.

6.2 Outstanding Issues

Despite the overall success of this work, some uncertainties related to its results remain. Some further research outside the scope of this work may be warranted in order to improve confidence in SNeuPI pressure measurement data.

The most significant outstanding issue is the question of whether or not the calculated I_{MCP} vs. pressure curves (Equations 5.1–5.3) accurately represent the physical reality of these relationships. Future researchers may wish to investigate the validity of this model, especially if similar instrument designs are to be flown on future satellite missions.

One possible approach to testing the validity of the pressure calibration curves may be to repeat the pressure calibration test using an electron source of known reliability and performance characteristics, such as a hot filament, rather than the Spindt emitter. The Spindt emitters used in testing throughout this work have frequently displayed erratic behavior and significant fluctuations in emission current magnitude over brief periods of time. Such behavior may potentially have contributed to inaccuracies in the derived I_{MCP} vs. pressure relationships.

Another matter worthy of further investigation is the inconsistent peaking behaviors evident

in the percent error plots presented in Sections 5.3 and 5.6. These behaviors may warrant efforts to determine the noise and accuracy characteristics of the laboratory test instruments utilized in this work. A better understanding of the performance of these instruments could enable greater confidence in the accuracy and precision of their measurements for future researchers.

Bibliography

MSIS E-90 Atmosphere Model. November 5, 2016. http://omniweb.gsfc.nasa.gov/vitmo/msis_vitmo.html.

NIST/SEMATECH e-Handbook of Statistical Methods. November 14, 2016. http://www.itl.nist.gov/div898/handbook/.

Analog Devices, Inc. (2002). *MAT03: Low Noise, Matched Dual PNP Transistor* (Rev. C ed.). Analog Devices, Inc.

Bayard, R. T. and D. Alpert (1950). Extension of the low pressure range of the ionization gauge. *Review of Scientific Instruments 21*(6), 571–572.

Burr-Brown (1998, May). *INA121: FET-Input, Low Power Instrumentation Amplifier*. Burr-Brown.

Catchpole, C. E. and C. B. Johnson (1970). Microchannel inverter image intensifiers and their use in electro-optical systems. In *Electron Devices Meeting, 1970 International*, Volume 16, pp. 44–46.

Clemmons, J. H., L. M. Friesen, N. Katz, M. Ben-Ami, Y. Dotan, and R. L. Bishop (2009). The ionization gauge investigation for the streak mission. *Space Science Reviews 145*(3), 263–283.

Colson, W., J. McPherson, and F. King (1970). Performance characteristics of a new high-gain imaging array. In *Electron Devices Meeting, 1970 International*, Volume 16, pp. 46–46.

Earle, G. D., A. M. Musumba, and S. L. Vadas (2008). Satellite-based measurements of gravity wave-induced midlatitude plasma density perturbations. *Journal of Geophysical Research: Space Physics 113*(A3). A03303.

Fowler, R. H. and L. Nordheim (1928). Electron emission in intense electric fields. *Proceedings of the Royal Society A: Mathematical, Physical and Engineering Sciences 119*(781), 173–181.

Garg, V. (2015, August). Swept Neutral Pressure Instrument (SNeuPI): Investigating gravity waves in the ionosphere. Master's thesis, Virginia Polytechnic Institute and State University, Blacksburg, Virginia.

Hanson, W., U. Ponzi, C. Arduini, and M. D. Ruscio (1992, July-September). A satellite anemometer. *The journal of the Astronautical Sciences 40*(3), 429–438.

Keithley Instruments, Inc. (2008). *Keithley Model 6220 DC Current Source Model 6221 AC and DC Current Source* (C ed.). Keithley Instruments, Inc.

Marquardt, D. W. (1963). An algorithm for least-squares estimation of nonlinear parameters. *Journal of the Society for Industrial and Applied Mathematics 11*(2), 431–441.

Noel, S. E. (2015, August). A framework for validation and testing of a cubesat retarding potential analyzer. Master's thesis, Virginia Polytechnic Institute and State University, Blacksburg, Virginia.

Photonis USA, Inc. (n.d.). *Advanced Performance Detectors*. 660 Main Street, Sturbridge, MA 01518: Photonis USA, Inc.

Sampson, M. J. (1998, October). Na-044: Tin whiskers. Parts advisory, NASA/Goddard Space Flight Center.

Spindt, C. A. (1968). A thin-film field-emission cathode. *Journal of Applied Physics 39*(7), 3504.

Spindt, C. A., I. Brodie, C. E. Holland, and P. R. Schwoebel (2001). *Spindt Field Emitter Arrays.*, pp. 105 – 186. John Wiley & Sons, Inc.

Texas Instruments Incorporated (2007, March). *LOG114: Single-Supply, High-Speed, Precision Logarithmic Amplifier*. Texas Instruments Incorporated.

Texas Instruments Incorporated (2015, April). *LMC6482 CMOS Dual Rail-to-Rail Input and Output Operational Amplifier* (Revision E ed.). Texas Instruments Incorporated.

Westerhoff, J., G. Earle, R. Bishop, G. R. Swenson, S. Vadas, J. Clemmons, R. Davidson, L. Fanelli, C. Fish, V. Garg, A. Ghosh, B. B. Jagannatha, E. Kroeker, P. Marquis, D. Martin, S. Noel, C. Orr, and R. Robertson (2015). Laice cubesat mission for gravity wave studies. *Advances in Space Research 56*(7), 1413 – 1427.

Appendix A

Additional Plots and Figures

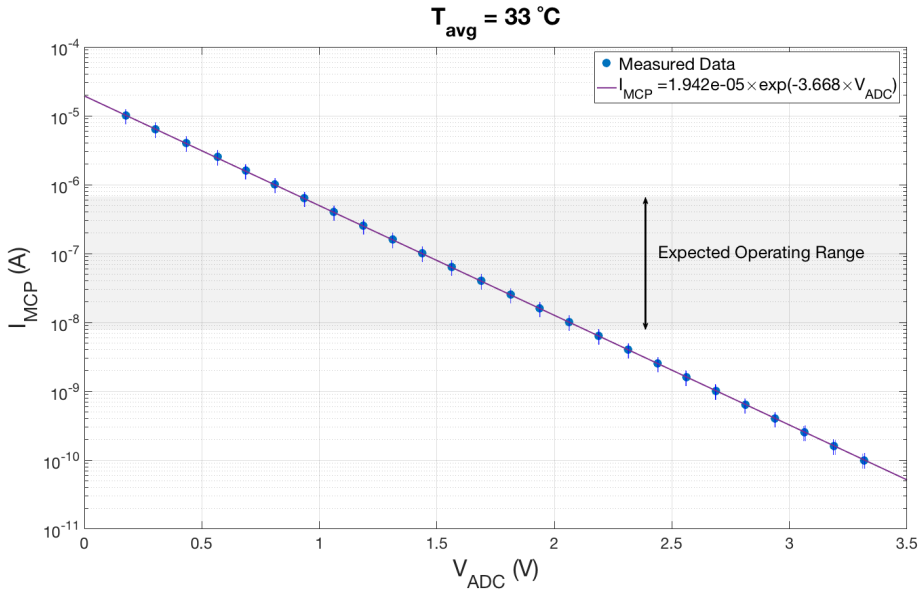

Figure A.1: Calibration curve for mean temperature of 33 °C. Error bar magnitudes are equal to two standard deviations of each V_{ADC} data point; note that error bar magnitudes are so small that only handles are visible. The best-fit line as calculated by MATLAB is shown in purple, and the range of expected operating input currents is shaded.

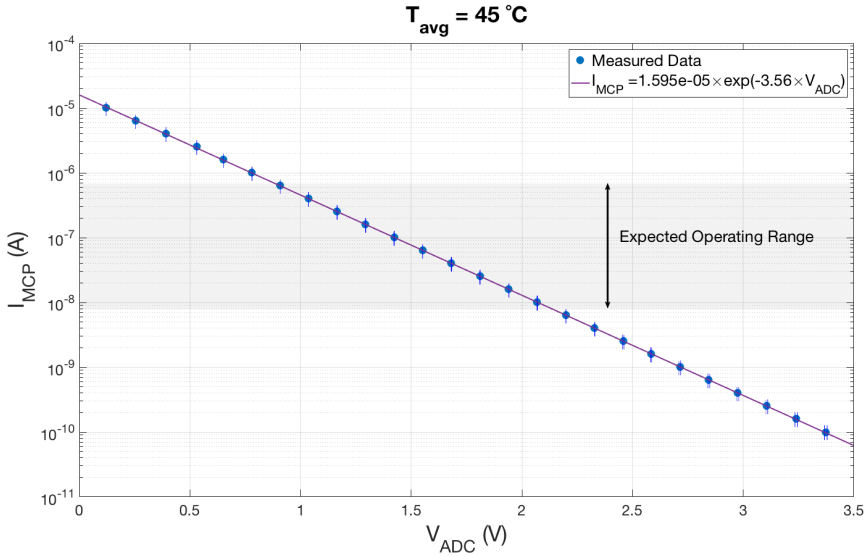

(a)

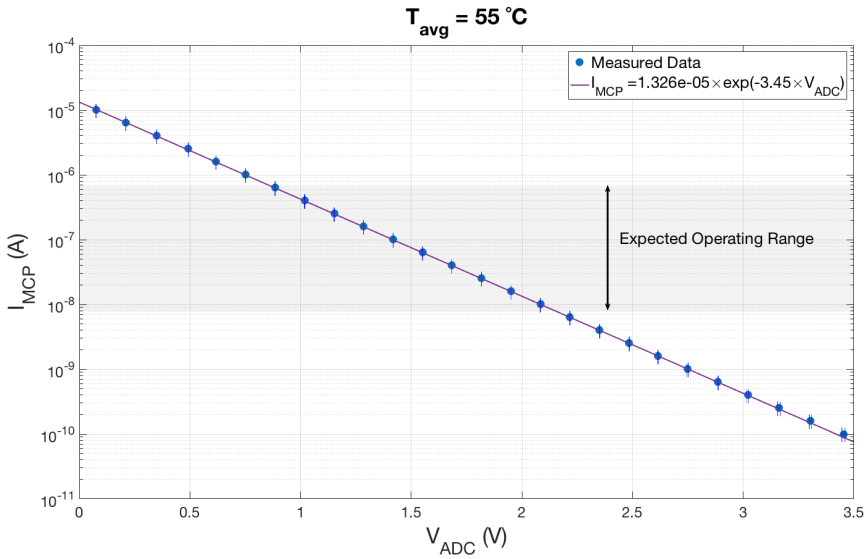

(b)

Figure A.2: Calibration curves for mean temperatures of 45 °C (a) and 55 °C (b). Error bar magnitudes are equal to two standard deviations of each V_{ADC} data point; note that error bar magnitudes are so small that only handles are visible. The best-fit lines as calculated by MATLAB are shown in purple, and the range of expected operating input currents is shaded.

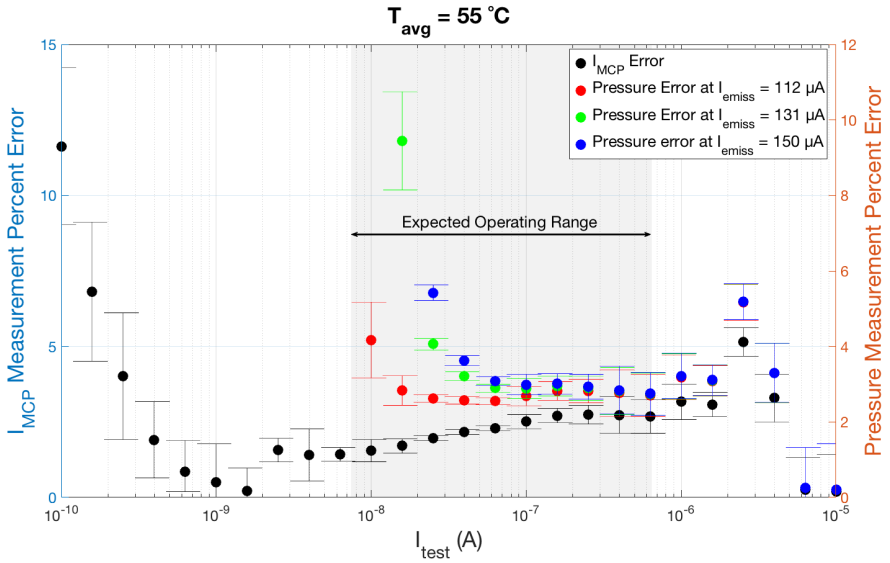

(a)

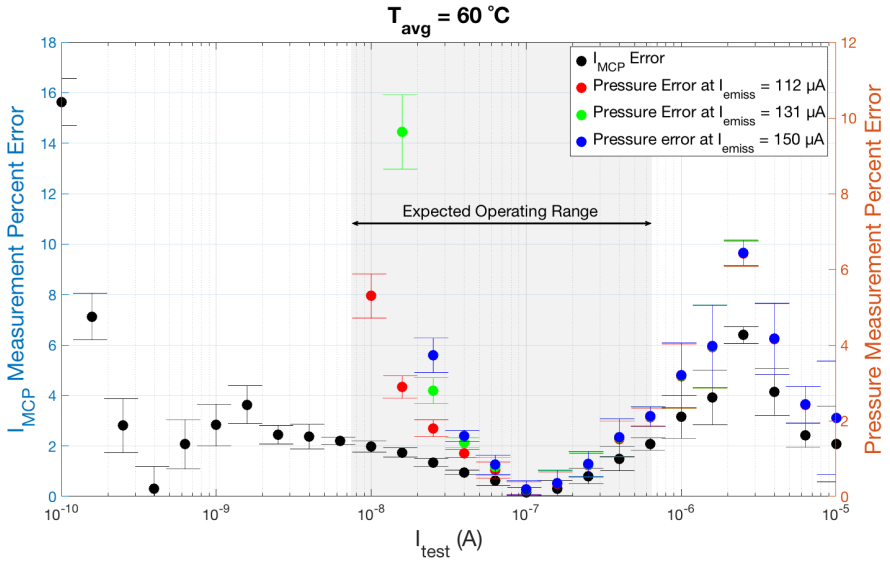

(b)

Figure A.3: Temperature compensated I_{MCP} measurement percent error vs. test current at 55 °C (a) and 60 °C (b). Error bar magnitudes correspond to an I_{MCP} measurement variability of two standard deviations.

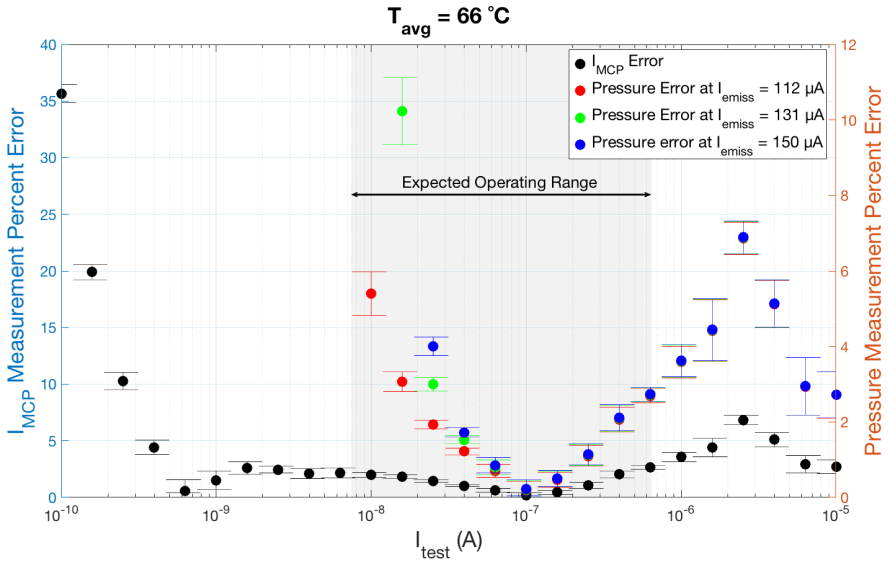

(a)

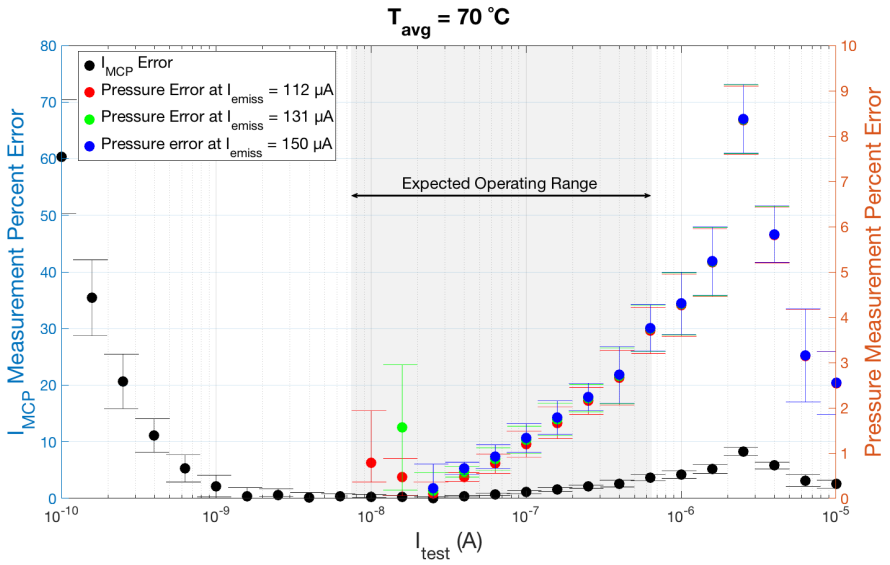

(b)

Figure A.4: Temperature compensated I_{MCP} measurement percent error vs. test current at 66 °C (a) and 70 °C (b). Error bar magnitudes correspond to an I_{MCP} measurement variability of two standard deviations.

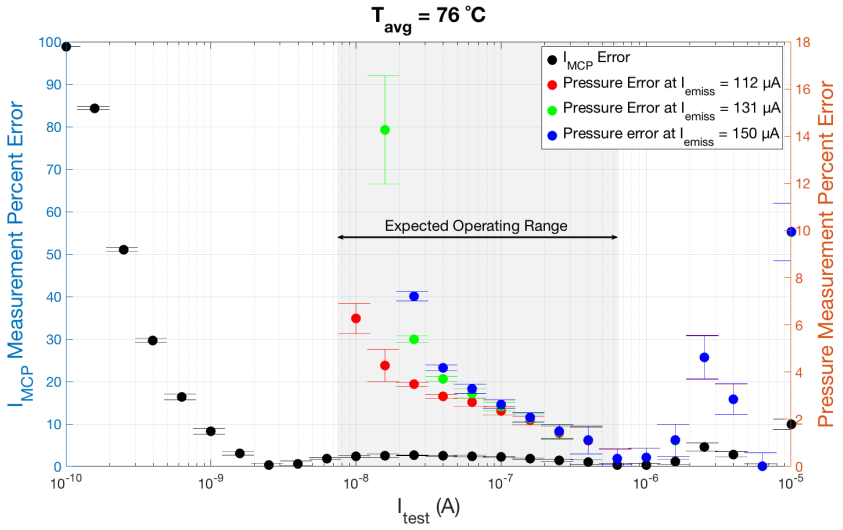

Figure A.5: Temperature compensated I_{MCP} measurement percent error vs. test current at 76 °C. Error bar magnitudes correspond to an I_{MCP} measurement variability of two standard deviations.

Appendix B

Additional Lessons Learned

B.1 Noise Considerations in Testing

Several unsuccessful attempts at testing the SNeuPI electrometer circuit were made before the test setup described in Chapter 4 was devised. One of the most important steps in collecting accurate test data proved to be ensuring adequate EMI shielding. The dataset in Figure B.1 was measured with the electrometer circuit inside the Space@VT vacuum chamber as previously described, but with the chamber door closed and the Keithley PCS output connected to an unshielded test lead passed through the chamber D-sub feedthrough. This arrangement had been devised with the intent of improving EMI shielding by closing the chamber door; however, significant deviation from logarithmic conformance was immediately evident on casual inspection of the data. The test was reattempted with the chamber door open to accommodate the triaxial shielded test lead normally used to connect the PCS output. The resultant test data had excellent logarithmic conformance.

It is worth noting that casual observation of the data in Figure B.1 would not necessarily implicate noise as the cause of poor logarithmic conformance if error bars were not present. One might, not unreasonably, suspect poor circuit design or component selection to have caused the deviation from the expected behavior. The lesson to be learned from this experience is that unexpected circuit behavior warrants careful examination of potential noise sources.

B.2 PCB Surface Contamination and Circuit Function

When dealing with very small signal currents, PCB surface leakage currents can have a detrimental effect on cicuit performance as well. The presence of flux residue or other contaminants on the surface of a board can have unpredictable effects.

No-clean flux is so named because its residue, in theory, presents a high enough impedance that it can be left on the surface of a PCB after soldering without the risk of significant

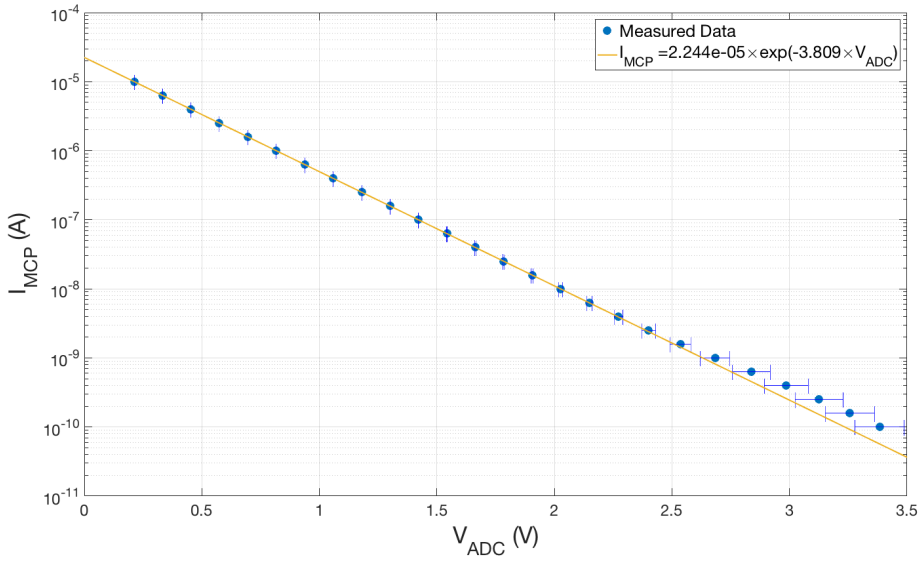

Figure B.1: Room temperature calibration sweep with unshielded PCS input lead. Note significant deviation from logarithmic conformance for lower range of input currents. This behavior is consistent between multiple datasets measured using this test setup. Calibration sweeps at higher temperatures display similar trends.

leakage current. Residue from easy-clean solder flux, on the other hand, while not as thick and difficult to remove as no-clean flux residue, must be removed in its entirety, as its impedance is low enough to cause significant leakage current problems. Figure B.2 shows a microscope image of a row of FPGA leads after being soldered to the SNeuPI FPGA PCB. A significant buildup of no-clean solder flux is visible on the PCB surface between the solder pads.

Both forms of flux were used in the population of the SNeuPI FPGA and electrometer PCBs. The solder paste used for the SMD components contains no-clean flux, and easy-clean flux was used for rework puposes. Although appropriate care was taken to flush the PCB surfaces with acetone immediately following the use of easy-clean flux, numerous circuit tests showed unpredictable behavior in the analog and digtal circuitry.

All of these problems were resolved after extensive and laborious cleaning of no-clean flux residue buildup from between components, pads, and traces. One potential explanation for this is that, during board rework, an amount of easy-clean flux residue sufficient to cause leakage current problems in some way permeated the no-clean flux residue already on the board. It is therefore recommended that the two types of solder flux not be used together in the population and rework of a single PCB.

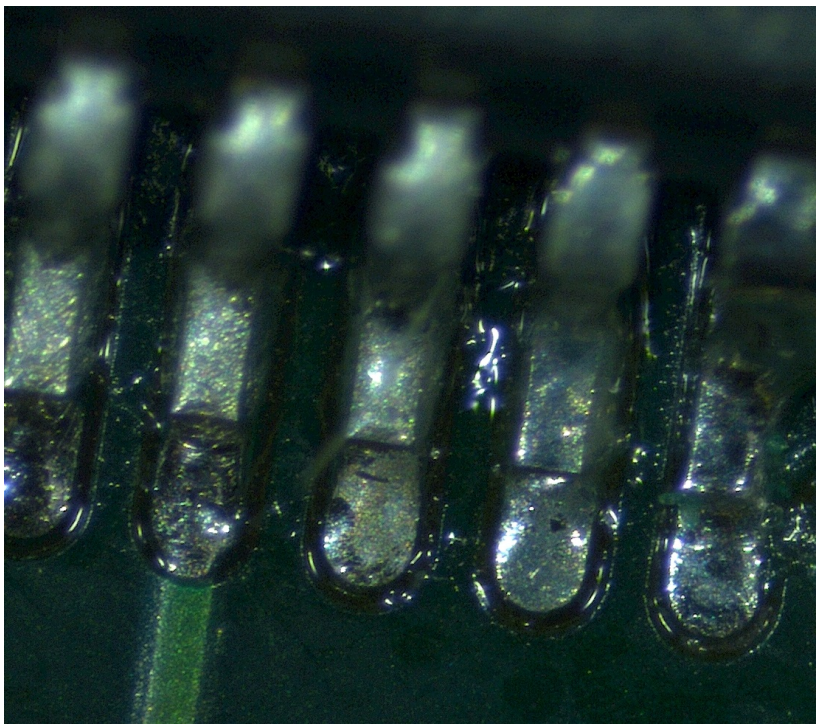

Figure B.2: Microscope image of SNeuPI FPGA pads post-soldering. Note visible accumulation of no-clean flux residue from solder paste.

Appendix C

Schematics and Electrometer Circuit Bill of Materials

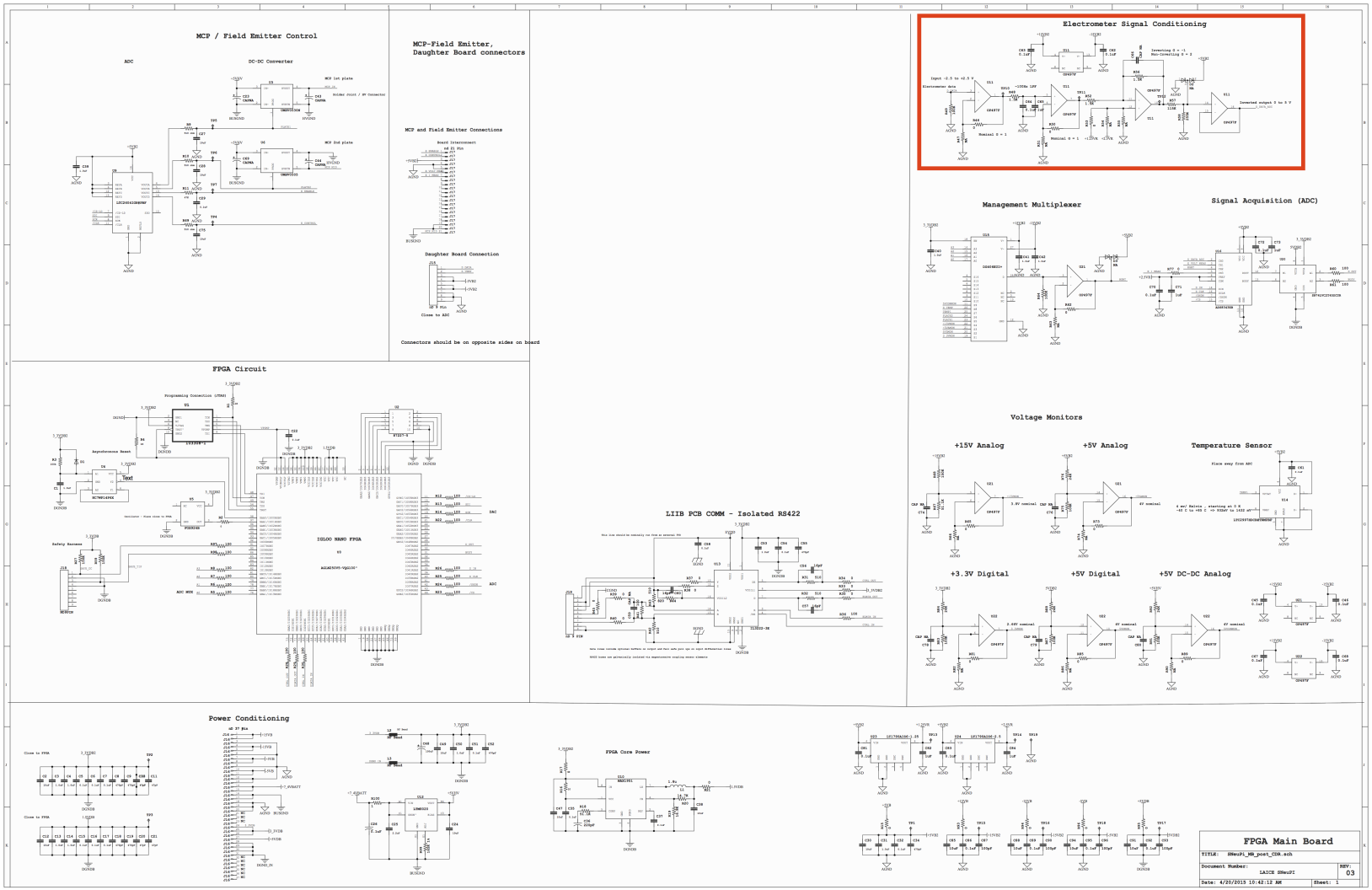

Figure C.1: FPGA board circuit schematic. The analog circuitry considered in the transfer function derivation in Section 3.1 is framed in red.

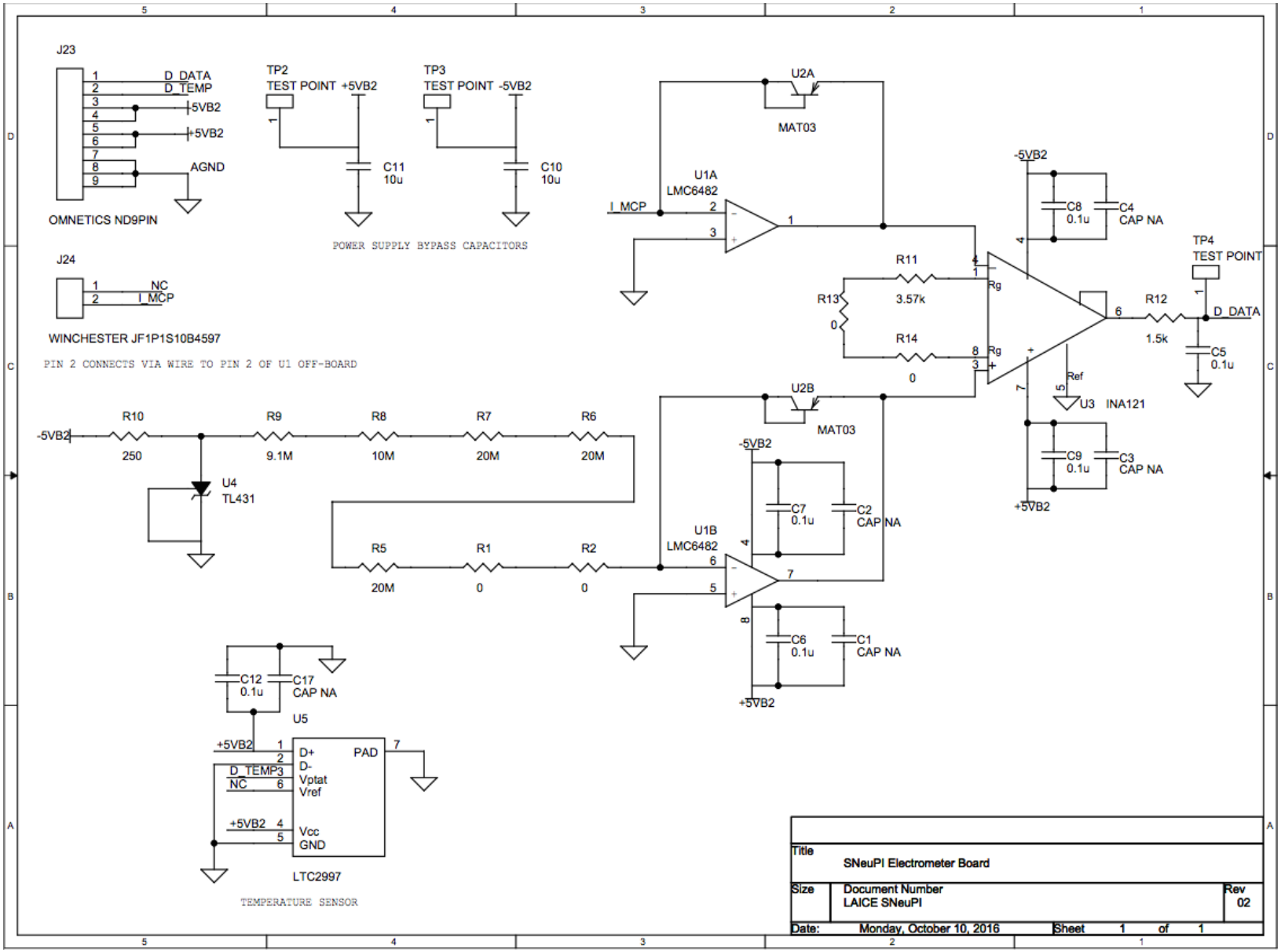

Figure C.2: Electrometer board circuit schematic.

Table C.1: Electrometer circuit bill of materials.

Reference	Qty	Value	Package	Manufacturer Part Number	Manufacturer	Description
C1, C2, C3, C4, C17	5	CAP NA	C0805			
C5, C6, C7, C8, C9, C12	6	0.1u	C0805	CGJ4J2X7R1E104K125AA	TDK Corporation	CAP CER 0.1UF 25V 10% X7R 0805
C10, C11	2	10u	C0805	C2012X5R1E106K085AC	TDK Corporation	CAP CER 10UF 25V 10% X5R 0805
J23	1	ND9PIN	ND9PIN	OMN9-A29400	Omnetics	9 Pin Connector Omnetics
R1, R2, R13, R14	6	0	R0805	MCU08050Z0000ZP500	Vishay Beyschlag	RES SMD 0.0 OHM JUMPER 1/5W 0805
R3, R4	2	1k	R0805	ERA-6AEB102V	Panasonic Electronic Components	RES SMD 1K OHM 0.1% 1/8W 0805
R5, R6, R7	3	20M	R1206	CRHV1206AF20M0FKE5	Vishay Dale	RES SMD 20M OHM 1% 0.3W 1206
R8	1	10M	R1206	RC1206FR-0710ML	Yageo	RES SMD 10M OHM 1% 1/4W 1206
R9	1	9.1M	R1206	RC1206FR-079M1L	Yageo	RES SMD 9.1M OHM 1% 1/4W 1206
R10	1	240	R0805	RMCF0805JT240R	Stackpole Electronics Inc.	RES SMD 240 OHM 5% 1/8W 0805
R11	1	3.57k	R0805	RN73C2A3K57BTDF	TE Connectivity AMP Connectors	RES SMD 3.57KOHM 0.1% 1/10W 0805
R12	1	1.5k	R0805	ERA-6AEB152V	Panasonic Electronic Components	RES SMD 1.5K OHM 0.1% 1/8W 0805
TP1, TP2, TP3, TP4	4	TESTPOINT	0.040" (1.02mm) Hole Diameter	5001	Keystone Electronics	TEST POINT PC MINI .040"D BLACK
U$3	1	KEYSTONE_1320	KEYSTONE_1320_STRAIGHT	11320	Keystone Electronics	Circuit Board Hardware - PCB .100 x .150 Solder Terminal
U1	1	LMC6482_7_LEAD	PDIP	LMC6482AIN/NOPB	Texas Instruments	IC OPAMP GP 1.5MHZ RRO 8DIP
U2	1	MAT03_5_LEAD	TO-78	MAT03EH	Analog Devices	Bipolar Transistors - BJT HIGH-SPEED DUAL PNP TRANS
U3	1	INA121P	PDIP	INA121P	Texas Instruments	IC OPAMP INSTR 600KHZ 8DIP
U4	1	TL431ACDBZRDIP-8	PDIP	TL431BIP	Texas Instruments	IC VREF SHUNT ADJ 8DIP
U5	1	LTC2997	DFN6	LTC2997HDCB#TRMPBF	Linear Technology	SENSOR TEMP RATIOMETRIC 6DFN
J24	1	JF1P1S10B4597	JF1P1S10B4597	JF1P1S10B4597	Winchester	JF series connector
N/A	2	20	R0805	RN73C2A20RBTD	TE Connectivity AMP Connectors	RES SMD 20 OHM 0.1% 1/10W 0805
N/A	2	10	R0805	RN73C2A10RBTD	TE Connectivity AMP Connectors	RES SMD 10 OHM 0.1% 1/10W 0805